STRATEGIES FOR COMPUTING THE SCALAR SELF-FORCE ON A
SCHWARSZCHILD BACKGROUND: A COMPARISON STUDY WITH AN FORTRAN
CODE IN C++, EXTRAPOLATING TO INFINITE DISCONTINUOUS GALERKIN
ORDER, AND EXTRAPOLATING TO INFINITE SPHERICAL HARMONIC MODES

A Thesis/Dissertation

Submitted to the Graduate Faculty of the
Louisiana State University and
Agricultural and Mechanical College
in partial fulfillment of the
requirements for the degree of
Master of Science

in

Physics

by
Steven (Susan) Dorsher
B.S., Massachusetts Institute of Technology, 2004
M.S., The Ohio State University, 2006
M.S., University of Minnesota, 2013
December, 2017

Acknowledgments

I would like to thank Peter Diener and Frank Löffler for their guidance. Peter Diener especially has been very important to me, both as an advisor and personally. Frank Löffler and the Einstein Toolkit grant has also provided some of the funding for this research, and I would like to thank him for that and for all of his help. I would also like to thank Gabriela Gonzalez for the excellent opportunity to work on LIGO during the time of three detections, which provided me the funding I needed to continue the work detailed in this document. I would like to thank Juana Moreno for the opportunity to work as outreach coordinator to the LA-SIGMA Research Experience for Undergraduates program my first summer at LSU, which also helped provide funding for this research. My parents, Paul and Joanne Dorsher, also deserve a mention, both for extraordinary moral support and for the financial support they provided that helped make this possible, as well as loving me endlessly and talking to me every single night. I'd like to thank my sister, Patricia Dorsher, my grandmother, Evie Dorsher, my Aunt Peggy Bennett, my Aunt Elaine Shirley, my Aunt Mary Brunbergy, and my friends Christy Paulson and Matt Ratliff, Hope Ring, Josh McKeown, and Adam for their steady presence in my life. I would also like to thank my workplace friends Peter Diener, Steven Brandt, Brad Schaefer, Frank Lóffler, Sreenath Vijayakumar, and Samuel Cupp for making work truly enjoyable, almost all of the time. My family, friends, and loved ones are the purpose behind this work.

Table of Contents

List of Tables

List of Figures

Abstract

Insert the text of your abstract here. Make sure there is one blank line between the end of the Abstract text and the "end" command below to maintain double–spaced lines.

Chapter 1
Introduction

1.1 Gravitational Waves

On February 11, 2016, the LIGO Scientific Collaboration announced the first detection of gravitational waves from a black hole binary inspirals, occurring on September 14, 2015, with pre-merger masses of 36 $M_\odot$ and 29 $M_\odot$ and a post merger mass of 62 $M_\odot$ at a redshift of $z = 0.09$ [34]. Two subsequent detections followed, on December 26, 2015 [35] and on January 4, 2017 [36], with masses that are about the same to within an order of magnitude.

There is a question of what is meant, observationally, by a black hole. Does it need to have a horizon? Does it need to have a Kerr metric (the simplest possible space-time for a spinning black hole in general relativity)? Does it simply need to be a sufficiently compact object that it can't be ordinary nuclear matter? Historically, black holes have been defined by their compactness [48]; however, some studies are beginning to consider tests of horizons [] or of the Kerr metric itself [48]. X-ray binaries, gravitational wave constraints from binary-pulsar systems, active galactic nucleii models containing super-massive black holes on the order of $10^6 M_\odot$, and the three LIGO detections, as well as black hole formation models, suggest that black holes of all scales should be spinning [48]. However, for the purposes of this manuscript, I will consider non-spinning, spherically symmetric black holes in general relativity, described by the Schwarzschild metric.

Currently, there are four distinct windows on the gravitational wave universe planned or in progress. The Laser Interferometer Gravitational Wave Observatory, LIGO, probably deserves first listing, due to their recent success. LIGO observes gravitational waves using a ground based Michelson-Morley interferometer with two 4 kilometer long Fabry-Perot cavity arms. It detects strains as small as $10^-23 Hz^{-1/2}$ [49].

1.2 Extreme Mass Ratio Inspirals

1.3 LISA

[15] [16] [11] [10]

1.4 Self force

EMfirst [9] circular orbits, spherical harmonics, world tube [?] gravitational DG wave eq, elliptical [?] 2nd order self force [21] MiSaTaQuWa? [18] basis for code [13]

1.5 Notation

In this manuscript, I use Einstein summation notation for tensors, where a repeated Greek index implies a summation over that repeated index. For example, an n dimensional tensor field of rank (1,2) transforms, in general, according to the rule

$$T^{\alpha}_{\beta\gamma}(\bar{x}^1, \ldots, \bar{x}^n) = \Lambda^{\alpha}_{\delta}\Lambda^{\epsilon}_{\beta}\Lambda^{\zeta}_{\gamma}T^{\delta}_{\epsilon\zeta}(x^1, \ldots, x^n) \tag{1.1}$$

where Λ is the jacobian of the coordinate transformation from x to $\bar{x}$.

Indices are raised by use of the inverse metric and lowered by use of the metric. The metric transforms contravariant one-forms, which constitute the basis, to covariant vectors, which constitute the coordinates, e.g. $u^{\beta} = g^{\alpha\beta}u_{\beta}$, where $g^{\alpha\beta}$ is the metric. However, the metric and its inverse can also be used to raise and lower indices of tensors of higher and mixed rank. The metric describes the relative distance between two coordinates on a manifold, in all n dimensions, in an $n \times n$ matrix. Two sign conventions are allowed, depending on whether the time component is positive or negative, though the metric always has a negative determinant in four dimensions. In our sign convention, the Minkowski

metric for flat spacetime is given by

$$
\eta^{\mu\nu} =
\begin{bmatrix}
-1 & 0 & 0 & 0 \\
0 & 1 & 0 & 0 \\
0 & 0 & 1 & 0 \\
0 & 0 & 0 & 1
\end{bmatrix}
$$

Here the four dimensions are Cartesian, t, x, y, and z. The Schwarzchild metric for a spherically symmetric blackhole without charge or spin is given by

$$
d\tau^2 = g^{\mu\nu}
\begin{bmatrix}
-(1 - \frac{2M}{r}) & 0 & 0 & 0 \\
0 & (1 - \frac{2M}{r})^{-1} & 0 & 0 \\
0 & 0 & r^2 & 0 \\
0 & 0 & 0 & r^2 \sin^2 \theta
\end{bmatrix}
$$

where $d\tau$ is the proper time, and coordinates are t (the local time), r (a radial coordinate that goes to zero at the singularity, $2M$ at the horizon, and infinity at spatial infinity), θ (the polar angle), and ϕ (the azimuthal angle). To obtain the inverse (lowered) metric, simply invert the matrix representation.

Chapter 2
A simple numerical solution for a PDE using the Discontinuous Galerkin method

2.1 Reduction to coupled first order differential equations

The fundamental problem we wish to solve is to evolve the wave equation on Schwarzschild spacetime with a source. However, to begin to address this problem, I implemented a one dimensional wave equation solver in C++ using the Discontinuous Galerkin method in flat spacetime. The wave equation in flat spacetime is given, in several different forms, by

$$\Box\psi = 0 \tag{2.1}$$

$$\frac{\partial^2\psi}{\partial t^2} = \nabla\psi \tag{2.2}$$

$$\frac{\partial^2\psi}{\partial t^2} = \frac{\partial^2\psi}{\partial r^2} \tag{2.3}$$

where the final form is specialized to one dimension. To numerically integrate this, it is necessary to reduce this second order differential equation to three coupled differential first order differential equations. There is a classical solution to this problem, which we follow. We introduce variables $\rho = \frac{\partial\psi}{\partial t}$ and $\phi = \frac{\partial\psi}{\partial r}$. With these definitions, and remembering that we want time evolution equations rather than spatial evolution equations, the three coupled equations become

$$\frac{\partial\psi}{\partial t} = \rho \tag{2.4}$$

$$\frac{\partial\rho}{\partial t} = \frac{\partial\phi}{\partial r} \tag{2.5}$$

$$\frac{\partial\phi}{\partial t} = \frac{\partial\rho}{\partial r} \tag{2.6}$$

4

This system of equations can be rewritten

$$\frac{\partial u}{\partial t} = A\frac{\partial u}{\partial r} + B\frac{\partial u}{\partial t} = RHS(u,t)$$

where u is the state vector consisting of $u = (\psi, \rho, \phi)$, and A and B are matrices. RHS stands for Right Hand Side. The C++ code has been implemented for wave equations of this generalized form, which encompases wave equations on a Schwarzschild spacetime.

2.2 Method of Lines

The method of lines is a method for solving partial differential equations in which spatial dimensions are discritized and time (conventionally) is evolved with numerical integration. We use this technique to solve the wave equation.

2.2.1 Spatial grids

Our code solves a wave equation, which must first calculate a spatial derivative then integrate in time to solve a differential equation. For the spatial derivative part of the scheme, we make use of the Discontinuous Galerkin method to compute spatial derivatives, as a replacement for a finite difference scheme. Its has three primary benefits. One is that it naturally handles discontinuities in the evolved field, which is important to the effective source approach that we use when calculating orbits with a source in curved spacetime. The second is that its accuracy scales exponentially with increasing polynomial order. The third is that its accuracy scales as a power law with decreasing element size, giving a second strong way to reduce the truncation error.

- **Finite difference schemes**

The classic solution to the spatial derivative problem is the finite difference scheme. In a one dimensional finite difference scheme, space is discretized into points on a line. The spatial derivative is calculated using a stencil of points that is symmetric about the point where one wants to know the spatial derivative, and extends $n - 1$ points beyond to either side, where n is the order of the expansion. The spatial derivative is calculated from a

5

weighted sum of the points included in the stencil, where some of the weights are negative. A stencil with $2n - 1$ points in it, in one dimension, corresponds to an nth order expansion. It is possible to expand any order of derivative to any order of expansion. A first derivative, to second order accuracy, given by:

$$D_r^{(2)} = \frac{1}{h}(-\frac{1}{2}f_{-1} + \frac{1}{2}f_1) \tag{2.7}$$

Here the f_{-1} and f_1 indicate the function evaluated at the grid point to either side of the 0th grid point, where the derivative is evaluated. Here h is the spacing between grid points. A first derivative, to third order accuracy, is given by:

$$D_r^{(3)} = \frac{1}{h}(\frac{1}{12}f_{-2} - \frac{2}{3}f_{-1} + \frac{2}{3}f_1 - \frac{1}{12}f_2) \tag{2.8}$$

Notice how no first order derivative includes the central point in its stencil. In contrast, a second derivative to second order accuracy is given by:

$$D_r'^{(2)} = \frac{1}{h^2}(f_{-1} - 2f_0 + f_1) \tag{2.9}$$

This derivative is symmetric, while the first derivative is antisymmetric.

It is possible to extend these stencils to two and three dimensions. When considering parallelization using OpenMP, issues of synchronization must be considered. When parallelizing over many nodes, the spatial grid gets divided into blocks. At the ends of each block, the boundary cells need information from the neighboring cells to calculate the spatial derivative. For an order n derivative, $n - 1$ boundary cells are synchronized into buffer zones both to the left and to the right at each time step. In our code, this is not necessary, since we have parallelized with OpenMP, which uses shared memory within one node, across several (16) cores.

- **The Disctontinuous Galerkin method**

The Discontinuous Galerkin method breaks space into segments called elements. Within each element, the value of the field is represented by the sum of n interpolating polynomials of order n, where n is the order of the element. There are $n + 1$ unevenly spaced nodes in the element, clustered toward the edges. At each node, exactly one of the interpolating polynomials takes on a value of one while the others are zero. An interpolating Lagrange polynomial has a functional form:

$$\ell_i(r) = \prod_{j=1, j \neq i}^{n} \frac{r - \xi_j}{\xi_i - \xi_j} \tag{2.10}$$

where ξ_i is a location of a node and where r is an arbitrary position [51].

Omitting the details of the derivation of this method, which can be found in Reference [51], the procedure for calculating the spatial derivative in one dimension is to first calculate the Legendre polynomials, rescaled by a factor depending upon their order. $\tilde{P}_n(r) = \frac{P_n(r)}{\sqrt{\gamma_n}}$ where $\gamma_n = \frac{2}{2n+1}$. The following procedure of differentiation and matrix inversion can be used to calculate the derivative matrix for each element, D_r [51].

$$V_{ij} = \tilde{P}_j(r_i) \tag{2.11}$$

$$V_{r,(i,j)} = \frac{d\tilde{P}_j}{dr}\big|_{r_j} \tag{2.12}$$

$$V^T D_r^T = (V_r)^T \tag{2.13}$$

In practice, we use a custom package, the Template Numerical Toolkit (TNT) library and JAMA, to invert the equation using LU decomposition. Beware! TNT and JAMA are not thread safe, and cannot be used with shared memory parallelization. They result in race conditions, and it was ultimately necessary to rewrite the parallelized portion of the code to avoid the TNT classes.

The Discontinuous Galerkin method helps damp error introduced by discontinuities in

7

the field, provided they remain at element boundaries. We make use of this in our self-force calculations in the neighborhood of the particle, to be described in Chapter 5.4. The numerical flux is a way of accounting for the discontinuity in the flow between neighboring elements. There are multiple ways of calculating this flux, but in our code, we use a version relevant to linear hyperbolic problems, such as Equation 2.7, which, recall, is specialized to a one-dimensional problem. In this case, $A = S\Lambda S^{-1}$, for some transformation matrix S, where Λ is a diagonal matrix. Let Λ^+ and Λ^- be the positive and negative eigenvalues of Λ, respectively, corresponding to the outgoing and ingoing waves. Then the numerical upwind flux is given by

$$(\hat{n}\dot{F}) = S(\Lambda^+ S^{-1} u^- + \Lambda^- S^{-1} u^+) \tag{2.14}$$

This flux, based upon the state vector interior to (u^-) and exterior to (u^+) the element, at each end of the element, is distributed across the whole element from end to end via the lift matrix [51].

2.2.2 Time evolution

Time evolution in our code is handled by a fourth order low storage Runga Kutta method. Instead of the standard fourth order Runga Kutta method, this method takes five sub-timesteps, but only the most recent sub-timestep needs to be stored.

$$p^{(0)} = u^n k^{(i)} = a_i k^{(i-1)} + \delta t RHS(p^{(i-1)}, t^n + c_i \delta t) p^{(i)} = p^{(i-1)} + b_i K^{(i)} u_h^{n+1} = p^{(5)} \tag{2.15}$$

Here steps two and three are repeated for $i = 1 - 5$, first k, then p, then increase i and repeat. The coefficients a_i, b_i, and c_i are given in Refence [51].

2.3 Wave equation on flat spacetime

Using gaussian initial conditions in ψ and setting the ρ initial conditions to the derivative of that gaussian, I have produced the evolution shown in Figure 2.1. The gausian marches to the right over a number of time steps, hits the periodic boundary conditions,
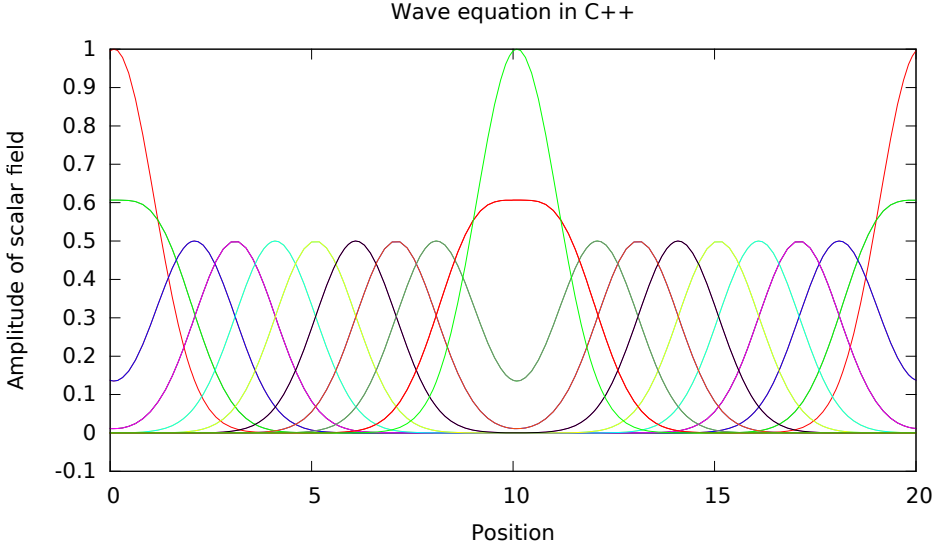
Figure 2.1: Waves evolving over time for gaussian initial conditions

and re-enters the one-dimensional space on the left, eventually returning to its original position. A similar progression can be seen in Figure 2.2 for sinusoidal initial conditions.

The Discontinuous Galerkin method has truncation error that scales as h^{n+1}, where h is the element size and n is the polynomial order of the elements. The L_2 error is definied as the square root of the sum of the squared differences across all space, after one complete cycle of the system. The scaling of the L_2 error with DG order and with element size is shown in Figures 2.3 and 2.4. The scaling matches expectations until roundoff error is hit, where the error stops improving with order or smaller element size. Not shown, this same partern was seen for the L_0 error, which is the maximum error over all space.

9
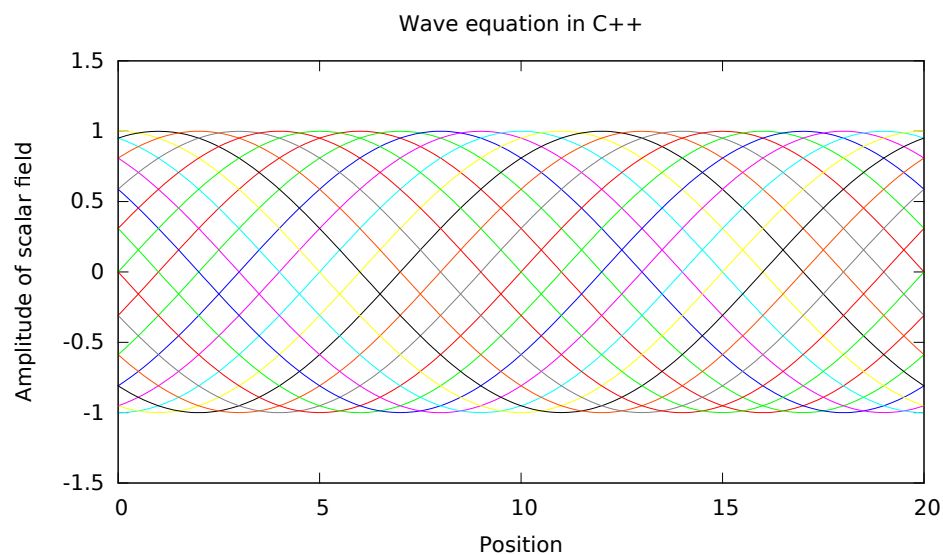
Figure 2.2: Waves evolving over time for sinusoidal initial conditions
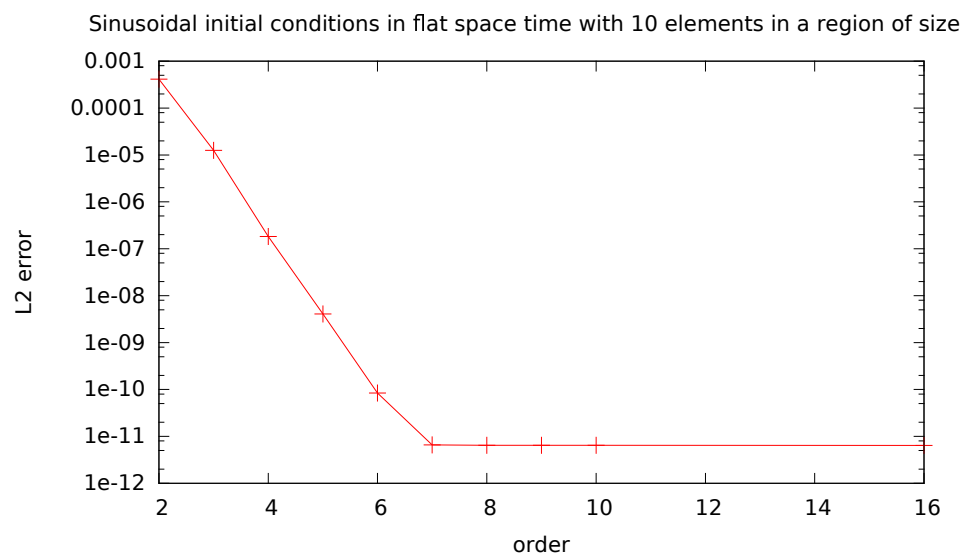
Figure 2.3: L_2 error scaling with DG order for sinusoidal initial conditions
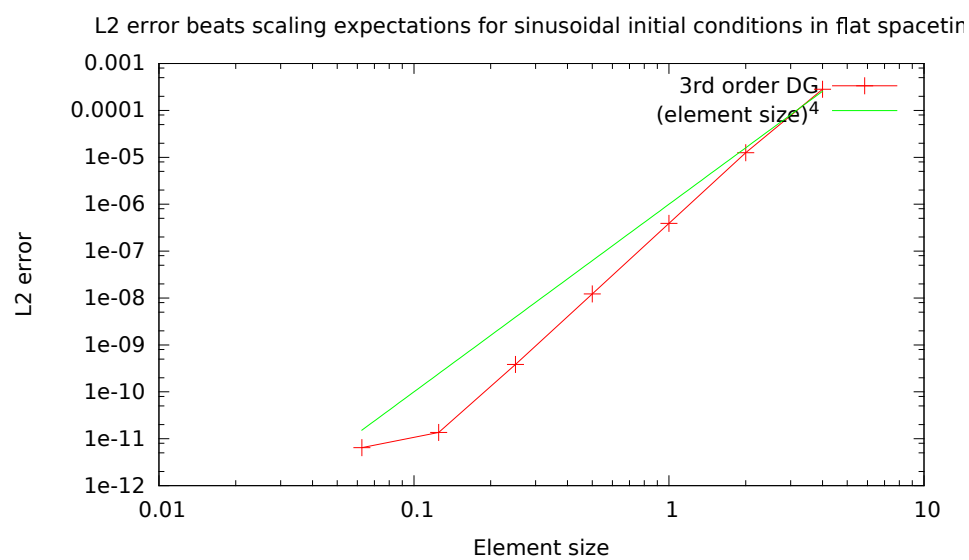
Figure 2.4: L_2 error scaling with element size for sinusoidal initial conditions

Chapter 3
A scalar field on a Schwarzschild background without a source

3.1 Scalar field on Schwarszchild spacetime

Although the final goal in this field is to compute tensor waveforms that can be used as templates for LISA searches, for the purposes of obtaining the desired accuracy, it is important to improve our computational methods. We do this by performing comparison studies using scalar, rather than tensor, self force methods to make the problem more tractible. I have performed the simplest of such comparison studies– I have reimplemented Peter Diener's Fortran scalar self-force code, with a slightly modified design, in C++. The desired goal was for the results to match to within roundoff error. This was achieved for scalar fields without a source and for scalar fields with point sources on circular orbits (see Chapter 4.3.

3.1.1 Scalar field wave equations

A scalar field is a field that has one one degree of freedom at a given point in space– rather than being a matrix, it has a single value. The scalar wave equation, on a Schwarzschild background,in the absence of a source, is, in its most abstract form, the same as in flat spacetime.

$$\Box \Psi = 0 \tag{3.1}$$

The details of the implementation are a little different, to account for the curvature of space. This enters through the metric. For a scalar field, the D'Alembertian can be written

$$\Box \Psi = \frac{1}{\sqrt{-g}} \partial_\mu (\sqrt{-g} \partial^\mu \Psi) = 0 \tag{3.2}$$

where g is the determinant of $g^{\mu\nu}$. [56]

- **Multipole moment decomposition**

  In our approach, spherical harmonics are used to reduce the three spatial dimensions to a one dimensional problem, in terms of the radius and a sum of an infinite number of discrete spherical harmonic modes, characterized by numbers l and m, where l ranges from 0 to ∞ and m ranges from $-l$ to $+l$ for each l [20]. The field is written as

$$\Psi = \sum_{l,m} \Psi^{lm}(t,r) Y^{lm}(\theta,\phi) \tag{3.3}$$

This separation of variables ansatz can be used to simplify the wave equation in any coordinate system, since the angular coordinates are not transformed in any of the coordinate systems we use. We make use of the identity

$$r^2 \nabla^2_{\theta,\phi} Y^{lm} = -l(l+1) Y^{lm} \tag{3.4}$$

where $\nabla^2_{\theta,\phi}$ is the angular part of the Laplacian, which has a $\frac{1}{r^2}$ dependence. This introduces a term proportional to $l(l+1)\Psi^{lm}(t,r)$ for each l, m.

- **Tortoise coordinates**

  In this code, we use a mixture of tortoise (Eddington-Finkelstein) and hyperboloidal coordinates. Tortoise coordinates have the property that they go to infinity at the horizon (scri minus) and infinity at lightlike infinity (scri plus). It is beneficial to place scri minus at an unreachable distance in coordinate space so that the boundary conditions at the horizon become trivial and there is no leakage of information from the interior of the blackhole to outside the horizon in the process of discritization. It is also beneficial to increase the number of computational elements near the horizon by compactifying the coordinates there. Tortoise coordinates transform only the radial coordinate, leaving the

angular and time coordinates alone. [56]

$$t_* = t \tag{3.5}$$

$$r_* = r + 2GM \ln |\frac{r}{2GM} - 1| \tag{3.6}$$

$$\theta_* = \theta \tag{3.7}$$

$$\phi_* = \phi \tag{3.8}$$

We solve the wave equation in tortoise coordinates in one region of the code. I have rederived this equation in Mathematica and verified the form that appears in Peter Diener's Fortran scalar self-force code. The wave equation in tortoise coordinates is

$$\frac{d^2\psi}{dt^2} = \frac{d^2\psi}{dr_*^2} - \frac{1}{r^5}(\frac{2M}{r} + (l+1)l)(1 - \frac{2M}{r})\psi \tag{3.9}$$

r is in Schwarszchild coordinates, r_* is in tortoise coordinates, l is the spherical harmonic l-mode (discussed below), which accounts for the angular dependence, and ψ is a function of tortoise coordinates.

- **Hyperboloidal coordinates**

  Hyperboloidal coordinates are necessary; however, because infinities are computationally unreachable. It is clear that space infinitessimally close to the horizon is important, since the curvature of space is strongest there, and it is still causally connected to the exterior region. To make the horizon reachable in a finite number of computational elements, while retaining the property that more computational elements are placed near the horizon than far away, hyperboloidal coordinates are introduced in the region closest to the horizon. In a middle region, tortoise coordinates are used. In the region furthest from the blackhole, hyperboloidal coordinates are used again to place scri plus at a finite number, yet maintaning the property that fewer computational elements are needed far away from the blackhole. Hyperboloidal coordinates are described by the transformation [14]

14

There are a few key features. The angular coordinates are not transformed. The time coordinate preserves the stationarity of the background metric, and thus the new time variable, τ, must be related to the old time variable, t_*, by an offset dependent only upon r_*, $\tau = t - h(r_*)$. For ingoing waves in the inner region, $t - r_* = \tau - \rho$ and in the outgoing region, $t + r_* = \tau + \rho$ to preserve the structure of the light cone. Bernuzzi, Nagar, and Zenginoglu define $H = \frac{dh}{dr_*}$. They introduce a compactification that depends on a window function Ω [19], such that the tortoise radius gets redefined $r_* = \frac{\rho}{\Omega(\rho)}$, resulting in an expression for the height function H in terms of the hyperboloidal radius, $H(\rho) = 1 - \frac{\Omega^2}{\Omega - \rho\Omega'}$. Their final wave equation, for ingoing waves, is [14]

$$\partial_t^2 - \partial_{r_*}^2 = -(1 - H^2)\partial_\tau^2$$
$$+(1 - H)(-2H\partial_\tau\partial_\rho + (1 - H)\partial_\rho^2 - (\partial_\rho H)(\partial_\tau + \partial_\rho)) \tag{3.10}$$

I have verified this equation, and derived the outgoing wave equation, in Mathematica.

- **Initial conditions and boundary conditions**

Since there is no source for the scalar field in the C++ code, it must be set to some initial value and allowed to fall into the blackhole or radiate away its energy to infinity. A gaussian initial condition in the time derivative of the scalar field, centered at computational coordinate zero (which was some physical distance outside the black hole horizon), was chosen. Initial conditions and the first timestep are shown in Figures **??**.

Boundary conditions were matched automatically by the coordinate transformation between tortoise and hyperboloidal layers. At scri minus and scri plus, the boundary conditions were that the scalar field be set to zero.

3.2 Theoretical expectations

The phase without a source is like the ringdown phase of the system. There are two analytically predicted behaviors that characterize the ringdown phase. After the plunge from the innermost stable circular orbit, quasinormal mode ringing begins. Eventually that
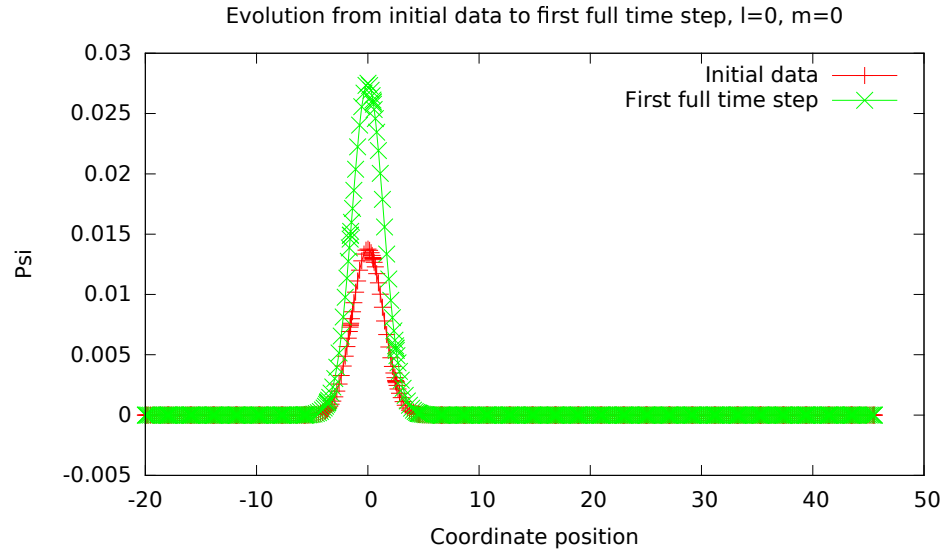
Figure 3.1: Scalar field spatial slice initial condition and first full timestep for l=0.
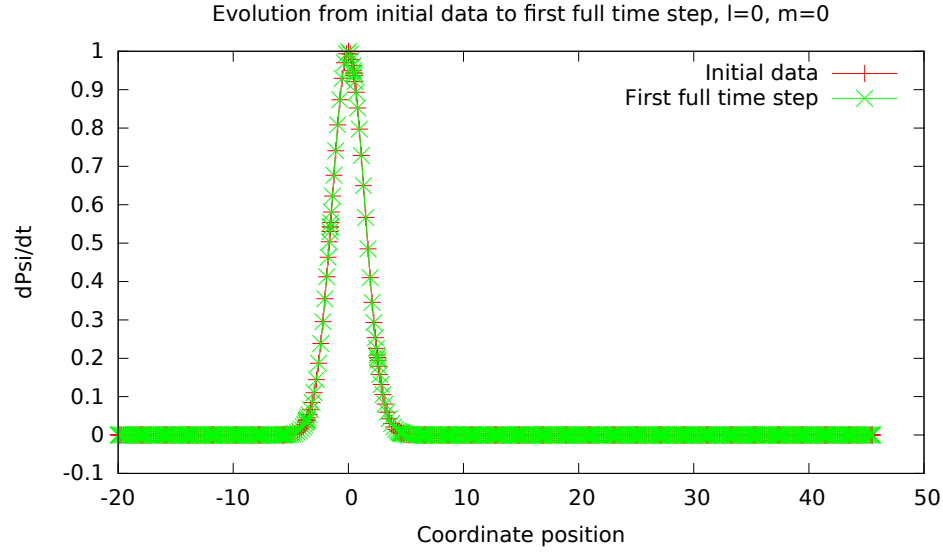
Figure 3.2: Time derivative of the scalar field spatial slice initial condition and first full timestep for l=0.
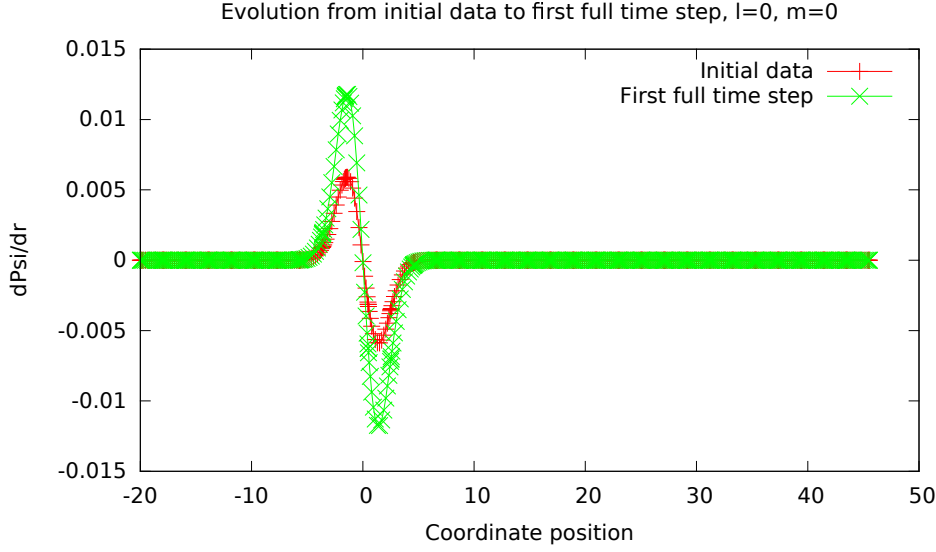
Figure 3.3: Radial derivative of the scalar field spatial slice initial condition and first full timestep for l=0.

fades into a long, power law tail.

3.2.1 Quasinormal modes

A field, such as a scalar or tensor field surrounding a blackhole, exhibits quasinormal mode ringing as it relaxes into or away from the blackhole. Hence, in LIGO, the first overtone of the first fundamental quasinormal mode was seen after the merger phase during the ringdown phase in LIGO's first detection [41]. In EMRI's, quasinormal modes are expected to be detected by LISA after the small black hole crosses the large blackhole's horizon, following the plunge from the innermost stable circular orbit. The same set of quasinormal modes is expected for any tensor field perturbed around a blackhole, regardless of why, as long as there is no ongoing source present. The case is very similar with scalar fields, though the spectrum of quasinormal modes is slightly different.

A quasinormal mode decays at a nearly stably frequency and a nearly steady exponential decay rate, with slight changes due to the loss of energy from the system. These rates have been calculated by Reference [5] and made available online. I have used their theoretical expectations for the first overtone at each l and m mode to fit my simulation data in Figures [?] and [?]. Notice that for higher m, the quasinormal mode frequency is

17
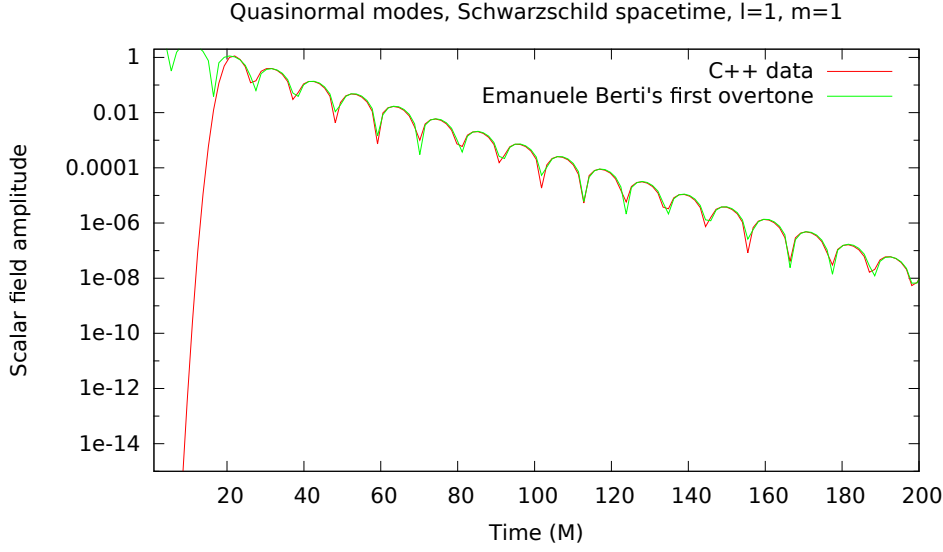
Figure 3.4: Quasinormal mode for l=1,m=1

higher and the decay is faster.

3.2.2 Power law tails

After quasinormal mode ringing settles down, power law tails begin. Both are due to backscattering of the waves off the background metric, but they take place in different regimes of time that has elapsed relative to perturbation initial conditions and background blackhole mass. In 1972, Richard Price predicted that the tails would scale as $t^-(2l+2)$ or $t^-(2l+3)$ depending on initial conditions [1]. In our choice of initial conditions, $t^-(2l+2)$ matches best for the choices of l explored. Figure 3.6 shows a mode for which I successfully recovered a power law tail. Figure 3.7 demonstrates that truncation error may dominate at high l, and that it may be necessary to increase the DG order to resolve all l-modes in a simulation.
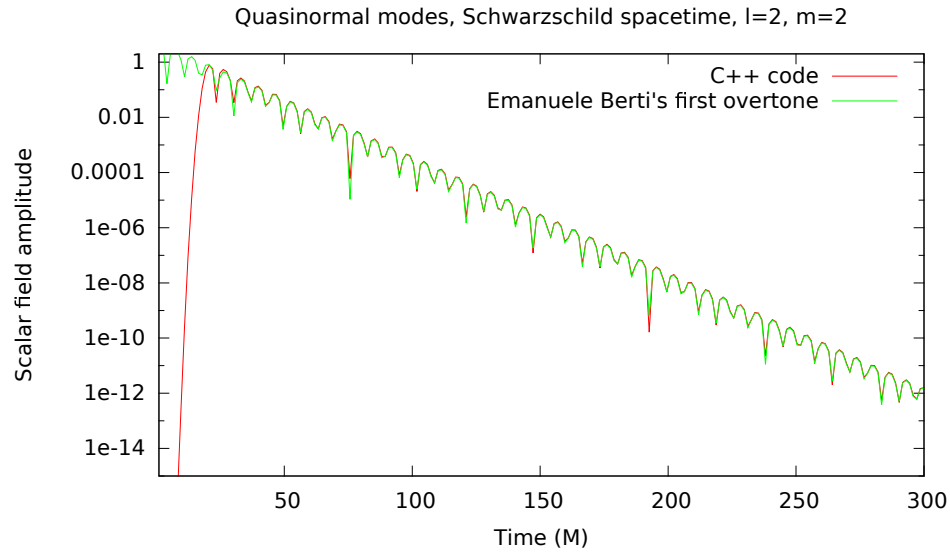
Figure 3.5: Quasinormal mode for l=2, m=2
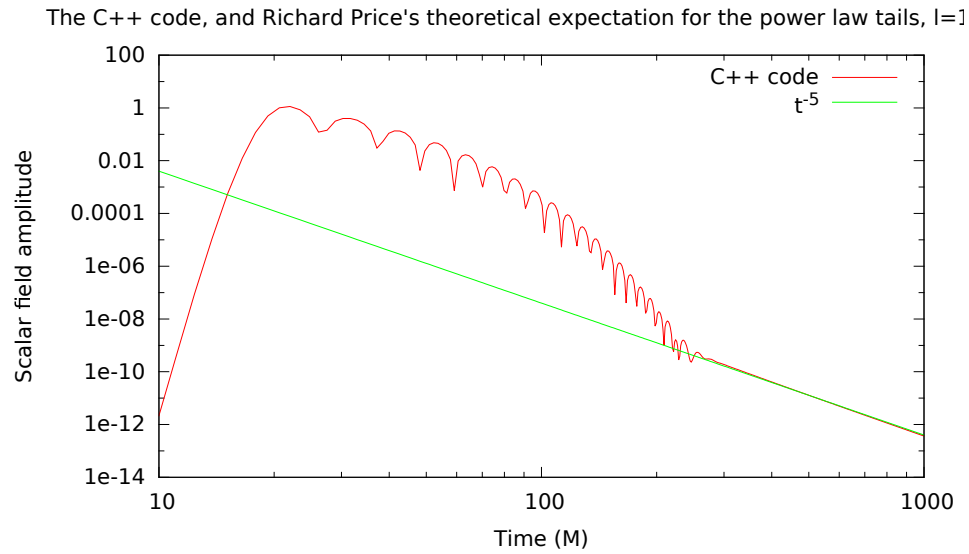
Figure 3.6: Power law tail, l=1, m=1
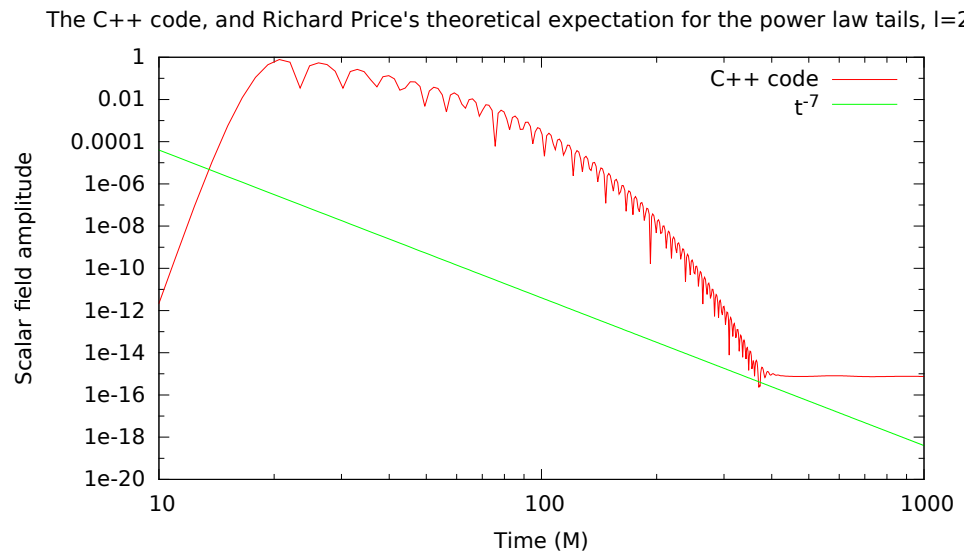
Figure 3.7: Power law tail does not match expectations due to truncation error in DG method, l=2, m=2

Chapter 4
Circular orbits on a Schwarzschild spacetime

4.1 Self Force

A test particle orbiting a blackhole follows a geodesic, which is the path of extremal proper time. This is described by the geodesic equation,

$$\frac{d^2 x^\mu}{d\tau^2} + \Gamma^\mu_{\rho\sigma} \frac{dx^\rho}{d\tau} \frac{dx^\sigma}{d\tau} = 0 \tag{4.1}$$

where τ is the proper time and $\Gamma^\mu_{\rho\sigma}$ is the Christoffel symbol, given by [57]

$$\Gamma^\sigma_{\mu\nu} = \frac{1}{2} g^{\sigma\rho} (\partial_\mu g_{\nu\rho} + \partial_\nu g_{\rho\mu} - \partial_\rho g_{\mu\nu}) \tag{4.2}$$

However, a blackhole, of any size, is not a test particle. In the limit of an EMRI, the additional force can be treated perturbatively in the mass ratio of the two particles, in the relativistic case. In the scalar case, the self force is simply written as a delta function source to the wave equation dependent upon the particle's position in time [32]

$$\Box \Psi^{ret} = -4\pi q \int \delta_4(x, z(\tau')) d\tau' \tag{4.3}$$

In this equation, $\Box$ is the D'Alembertian and $z(\tau')$ is the evolving path of the source in spacetime as a function of the particle's proper time. The retarded field Ψ^{ret}, is defined to be the field determined by physics taking place at $t_r = t - \frac{|\vec{r}-\vec{r}'|}{c}$; that is, at some distance away from the particle's path, the physical effects of gravity on the scalar field are retarded by light travel time. In the scalar approximation, the particle acts as a delta function point source, with a charge of q and mass m. That charge may accelerate or evolve with time; see chapter 8.3.
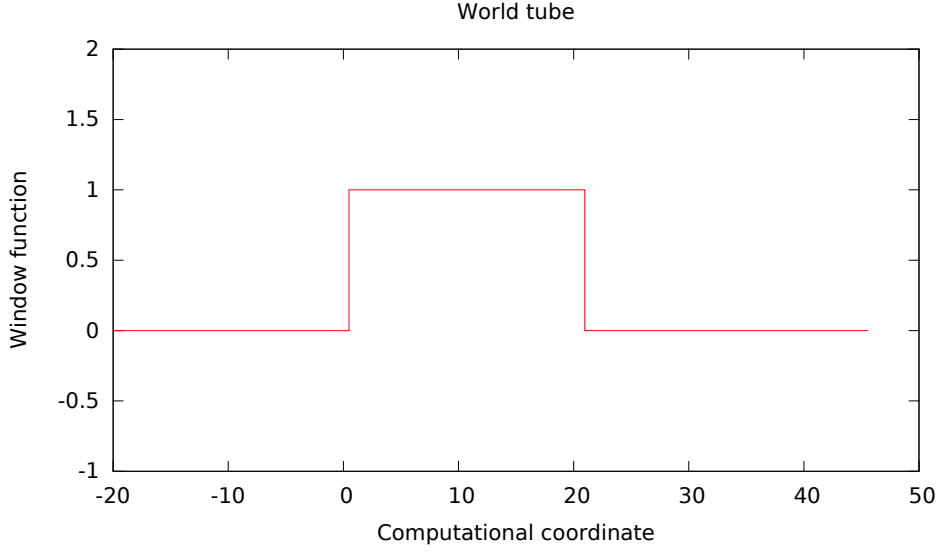
Figure 4.1: Spatial slice of the world tube window function.

The retarded field is singular at the location of the particle due to the delta function source. Singularities are computationally problematic. To regularize this singularity, a regular field is created through the use of an effective source.

$$\Psi^R = \Psi^{ret} - \Psi^S \tag{4.4}$$

$$\Box \Psi^R = S_{eff} \tag{4.5}$$

$$S_{eff} = q\delta(x, x_0) - \Box(W\Psi^S) \tag{4.6}$$

$$F_\alpha = (\nabla_\alpha \Psi^r)|_{x=x_0} \tag{4.7}$$

The regularized field, Ψ^R, is defined in terms of the retarded field with the singular field, Ψ^S, subtracted. This leads to the definition of an effective source, S_{eff}, that is zero inside the neighborhood of the particle, due to the world tube window function around the particle, shown in Figure 4.1, and that approximates the source outside that region. Outside that region, the regularized field is equal to the retarded field. The self-force can be derived from the final equation given above, F_α is merely a gradient of the field itself [?].

22

4.2 World tube

The world tube window function around the particle carves out a ring around the blackhole in the orbital plane, due to the use of spherical harmonics to increase the dimensionality of space. In my C++ code, the world tube extends throughout the entire tortoise region, ending at the transitions to the hyperboloidal regions. When calculating numerical fluxes at this boundary, it is necessary to account for both the coordinate transformations between either side of the boundary and the transformation between regular and retarded field.

While on a circular orbit, the particle follows a fixed path that prevents it from inspiraling. This does not conserve energy, since energy is radiated away into the blackhole and to infinity by the scalar waves. Clearly, we are artificially inputting energy into the simulation by holding the particle fixed on its orbit. This, in a nutshell, explains the need for scalar (or gravitational) radiation, and for self force in this limit.

4.3 Comparison between C++ and Fortran codes

I've performed extensive comparisons between Peter Diener's Fortran code **??**, implementing the same thing, and my C++ code. To roundoff precision, they agree, as evidenced by the near-machine-precision (10^{-15}) levels of agreement in both absolute and relative error that I achieve in Figures 4.2, 4.3, 4.4, and 4.5
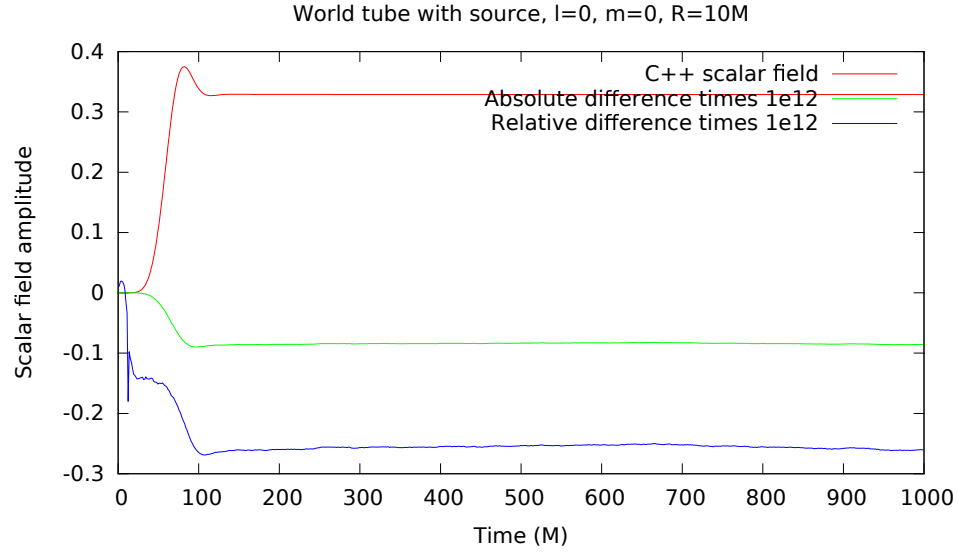
Figure 4.2: Comparison between Fortran and C++ codes for a particle on a circular orbit, l=0, m=0.
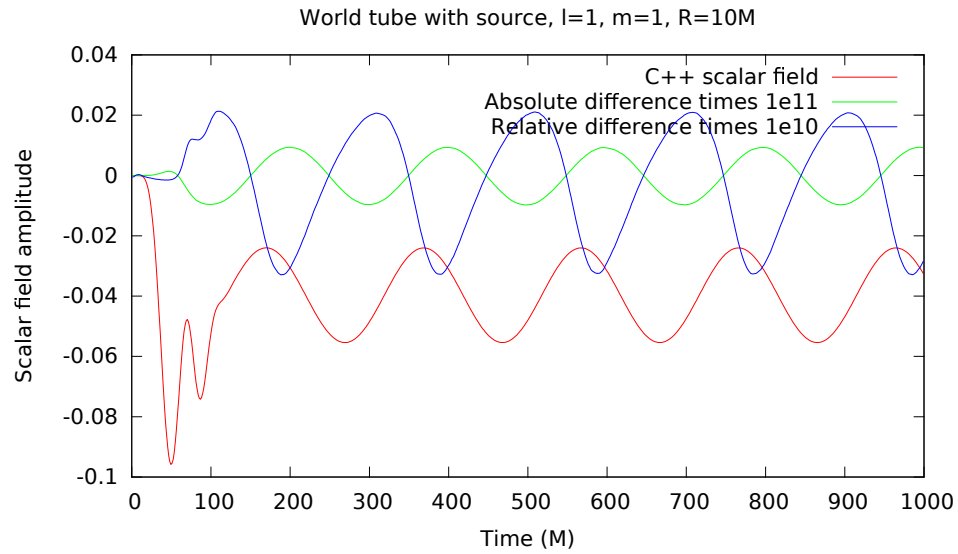
Figure 4.3: Comparison between Fortran and C++ codes for a particle on a circular orbit, l=1, m=1.
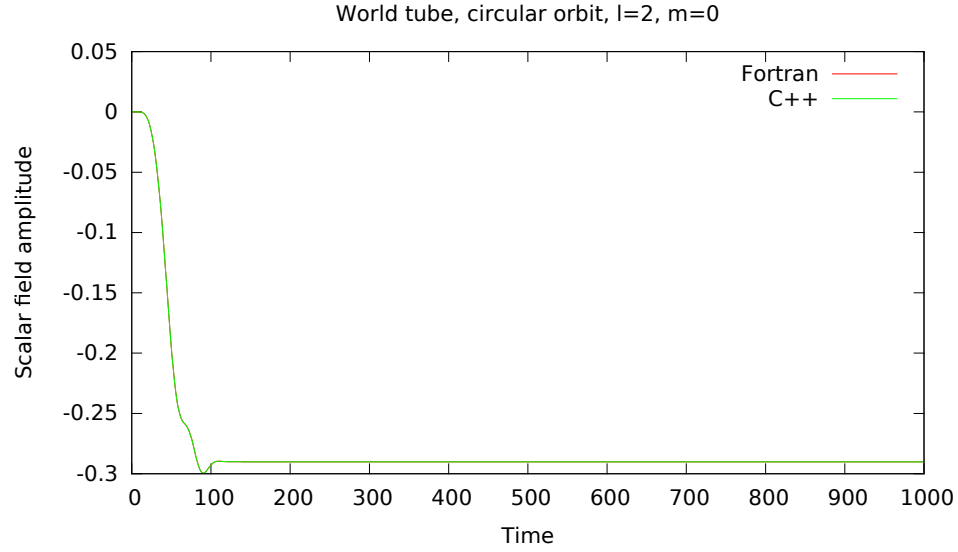
Figure 4.4: Comparison between Fortran and C++ codes for a particle on a circular orbit, l=2, m=0.
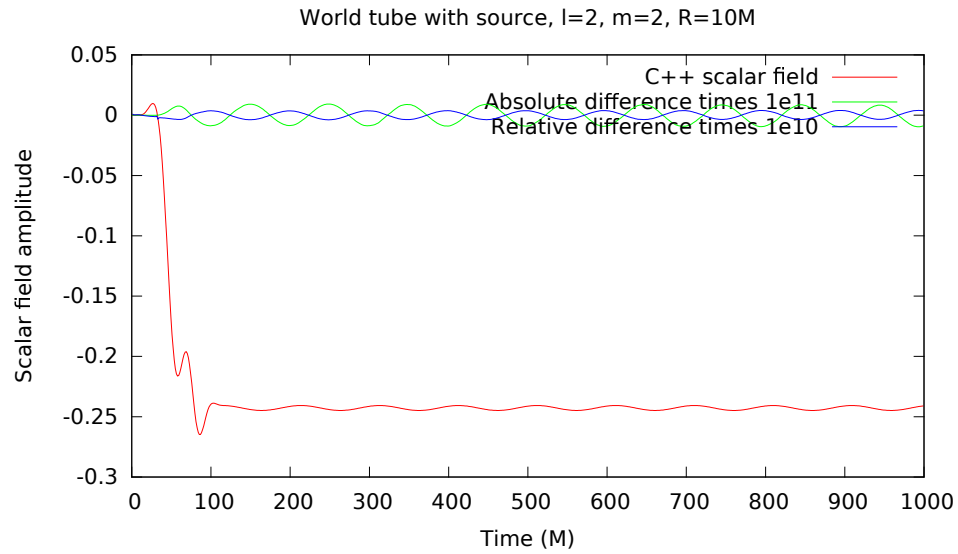
Figure 4.5: Comparison between Fortran and C++ codes for a particle on a circular orbit, l=2, m=2.

Chapter 5
Elliptical orbits on a Schwarzschild spacetime

For eliptical orbits, there are two primary additional physical or computational effects to consider. One is the need for ellitpical orbit paramters, expressed in terms of an eccentricity and a semilatus rectum, determined by an energy and an angular momentum. The second is the addition of a time dependent coordinate transformation region between tortoise layers in the middle of the computational grid, containing the position of the particle for all times. In this section, I describe Peter Diener's Fortran code, using Niels Warburton's exact initial conditions for l-modes 0 through 5, and Barry Wardell's effective source, which I have run to produce elliptical orbit output. Similar computations have been done before, using the Discontinuous Galerkin method, by Reference **??**, for the gravitational tensor field case; however, the scalar Discontinuous Galerkin case is not yet published.

5.1   Orbital parameters

The orbital parameters of an elliptical orbit in a Schwarzchild spacetime are defined through the following conditions.

$$E^2 = \frac{(p-2-2e)(p-2+2e)}{p(p-3-e^2)} \tag{5.1}$$

$$L^2 = \frac{p^2 M^2}{p-3-e^2} \tag{5.2}$$

Here, E is the energy and L is the angular momentum. e is the eccentricity and p is the semilatus rectum, which is a dimensionless measure of half the "width" of the elliptical orbit. More clearly, $r_{periastron} = \frac{pM}{1+e}$ and $r_{apastron} = \frac{pM}{1-e}$. χ is a parameter that runs from 0 to 2π in one radial cycle (as opposed to ϕ, which runs from 0 to 2π in one angular cycle).

In terms of these parameters [23],

$$r'(\chi) = \frac{pMe\sin(\chi - w)}{[1 - e\cos(\chi - w)]^2} \tag{5.3}$$

$$\phi'(\chi) = \sqrt{\frac{p}{p - 6 - 2e\cos\nu}} \tag{5.4}$$

$$t'(\chi) = \frac{p^2 M}{(p - 2 - 2e\cos\nu)(1 + e\cos\nu)^2}$$

$$\frac{d\chi}{dt} = \left(\frac{dt}{d\chi}\right)^{-1} \tag{5.5}$$

where $\nu = \chi - w$. For an elliptical orbit, χ and ϕ are evolved using a fourth order Runga Kutta integration using the oscillating orbits framework described in Reference **??**. For a self consistent evolving orbit with the backreaction effect of the self-force, see future work in Chapter 8.3.

5.2   Time dependent coordinate transformation

In the case of an elliptical orbit, it is necessary to ensure that the particle always remains within the tortoise region, so that the effective source remains valid. We use a time dependent coordinate transformation to keep the particle fixed at a specific coordinate location while the space in its immediate neighborhood evolves. With the proper boundary conditions, enforced by the numeric flux, this simulates a particle on an elliptical orbit and produces the same self-force and the same scalar waves at scri plus. The necessary time dependent coordinate transformation can be found in Reference [26]. It transforms from tortoise coordinates, ξ, to time dependent coordinates, x. The location of the particle $\xi_p(t)$, varies in tortoise coordinates but is fixed in time dependent coordinates (x_p). a and b are the boundaries of the time dependent region, in computational coordinates.

$$x = a + \frac{x_p - a}{\xi_p - a}(\xi - a) + \frac{(b - \xi_p)(\xi_p - a) - (x_p - a)(b - \xi_p)}{(\xi_p - a)(b - \xi_p)(b - a)}(\xi - a)(\xi - \xi_p) \tag{5.6}$$

I have used Mathematica to confirm the time dependent coordinate wave equation used in Peter Diener's Fortran scalar self-force code. Its time and radial components are

$$\frac{d^2\psi}{dt^2} = \left(\frac{dx}{d\xi}\right)^{-3}\left[\frac{d^2x}{d\xi^2} - \frac{d^2x}{d\xi^2}\left(\frac{dx}{dt}\right)^2 - 2\frac{d^2x}{d\xi dt}\frac{dx}{d\xi} - \left(\frac{d^2x}{dt^2}\right)^2\right]\frac{d\psi}{d\xi}$$
$$+\left[-1 + \left(\frac{dx}{dt}\right)^2\right]\left(\frac{dx}{d\xi}\right)^{-2}\frac{d^2\psi}{d\xi^2}$$
$$-2\frac{dx}{dt}\left(\frac{dx}{d\xi}\right)^{-1}\frac{d^2\psi}{d\xi dt} \qquad (5.7)$$

It is necessary to invert the time dependent transformation and subtract the singular field from the scalar field (and its derivatives) to obtain ingoing fluxes at elements just outside the world tube. Similarly, to obtain ingoing fluxes inside the world tube, we must transform to time dependent coordinates and subtract the singular field from the scalar field. For outgoing fluxes, addition and subtraction are reversed.

5.3 Orbits

I have computed four orbits of the system, at DG order 44. Figure 5.1 shows the radius iin Schwarzschild coordinates as a function of time. Figure 5.2 shows the sense in which this orbit is elliptical– if it did not precess, it would form an ellipse. Figure 5.3 depicts the physical path of the orbit, including precession. Figure 5.4 demonstrates why precession must exist. The periods of the angular variable ϕ and the parameter that governs the rate of radial evolution, χ, are not synchronized.

5.4 Self force output

The radial self-force is defined as $q\nabla^\alpha\Psi^R$ [?]. To compute this self force, it is necessary to sum over all l and m modes. In principle it is necessary to sum to $l = \infty$. Figures 5.5, 5.6, and 5.7 are computed using a fit to extrapolate to infite l, based on an analytic sum of the remaining terms after the highest l-mode computed. See Chapter ?? for details of the mode sum. Two terms of the sum described in that chapter were used in the fit.
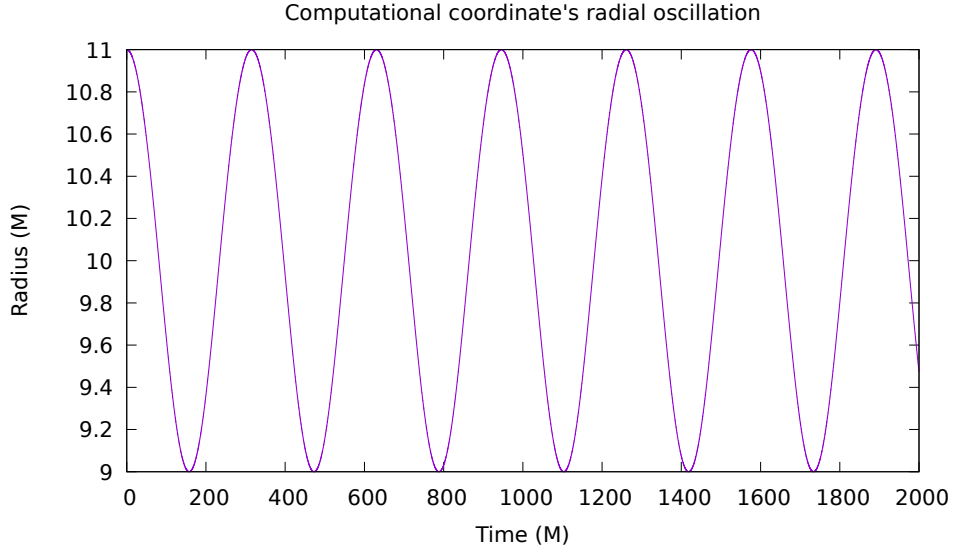
Figure 5.1: Schwarszchild r as a function of time over several orbits.
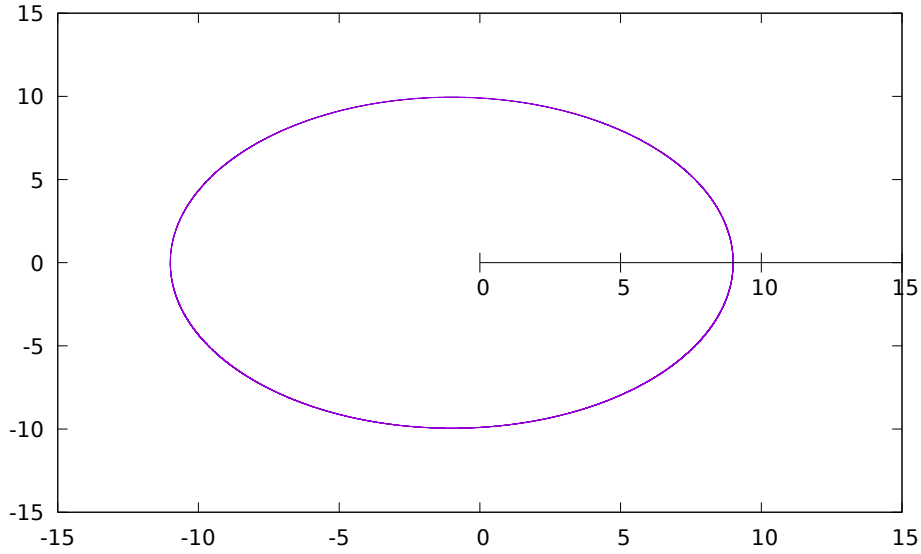
Figure 5.2: With χ as the angle in polar coordinates, the orbit forms an exact ellipse. This is the definition of χ, provided r is in Schwarzschild coordinates. Shown for $p = 9.9$ and $e = 0.1$, DG order 44
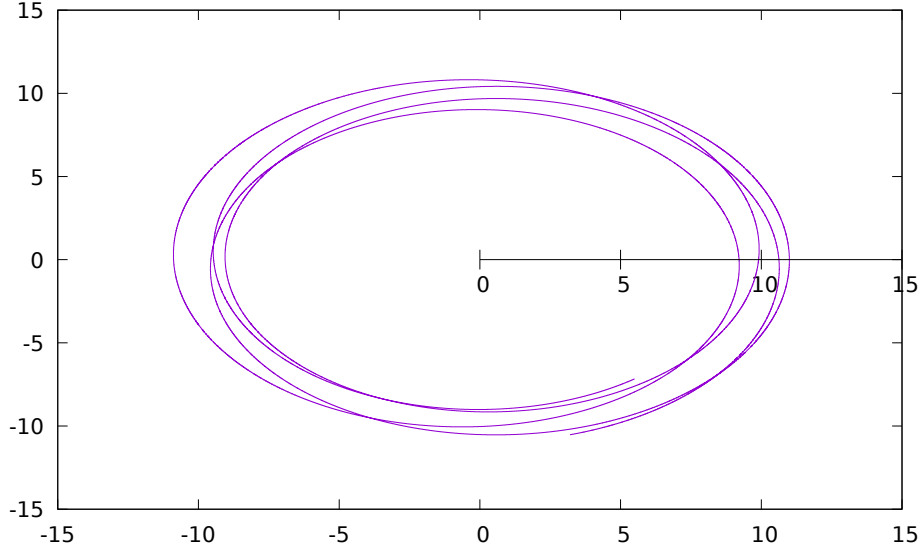
Figure 5.3: The orbit as it physically would exist, using Schwarzschild ϕ as the polar coordinate angle. The orbit precesses but does not inspiral since there is no generic evolution. Shown for $p = 9.9$ and $e = 0.1$, DG order 44
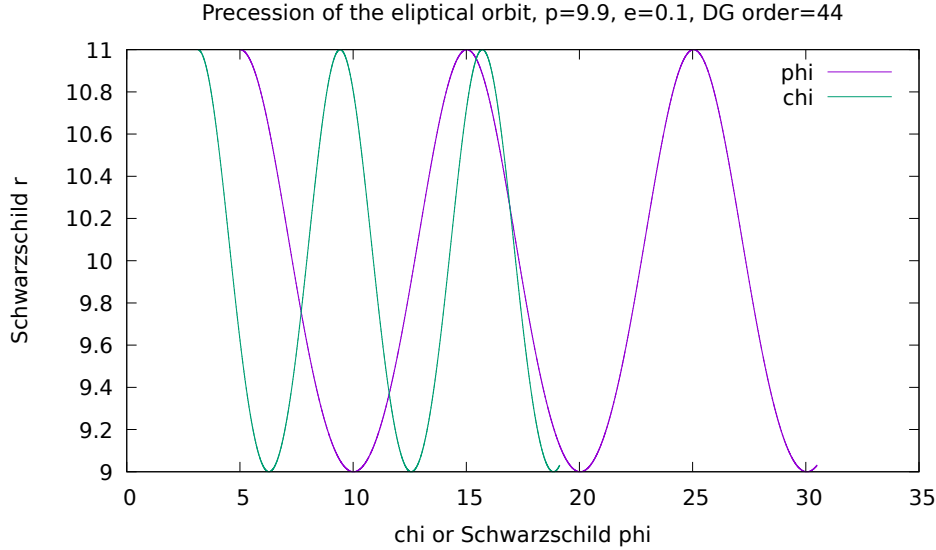
Figure 5.4: Precession of the eliptical orbit is demonstrated due to the inequality in the period of the angular variables χ, which represents the period of the radial oscillations, and ϕ, which represents the period of the angular oscillations. $p = 9.9$, $e = 0.1$, DG order 44.
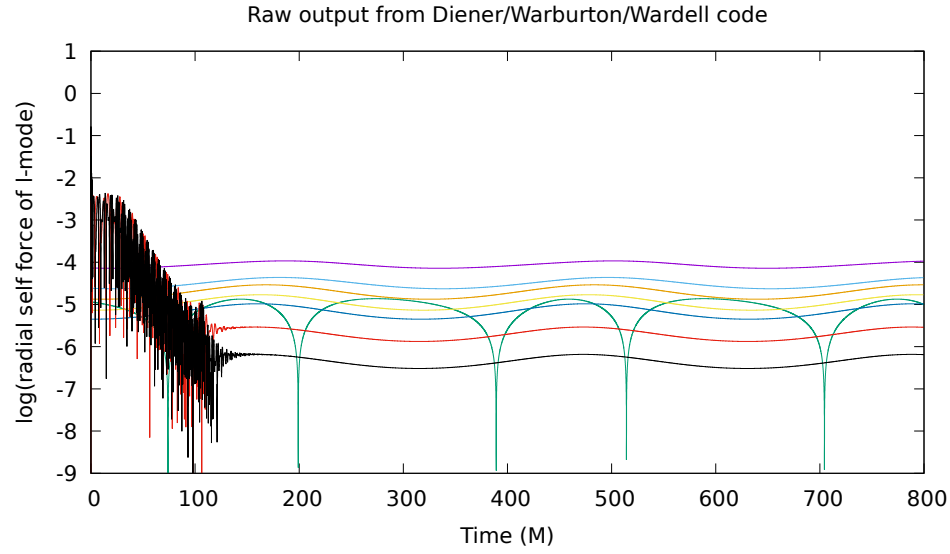
Figure 5.5: Raw output of Diener, Warburton, and Wardell code for DG order 44. Radial self force.
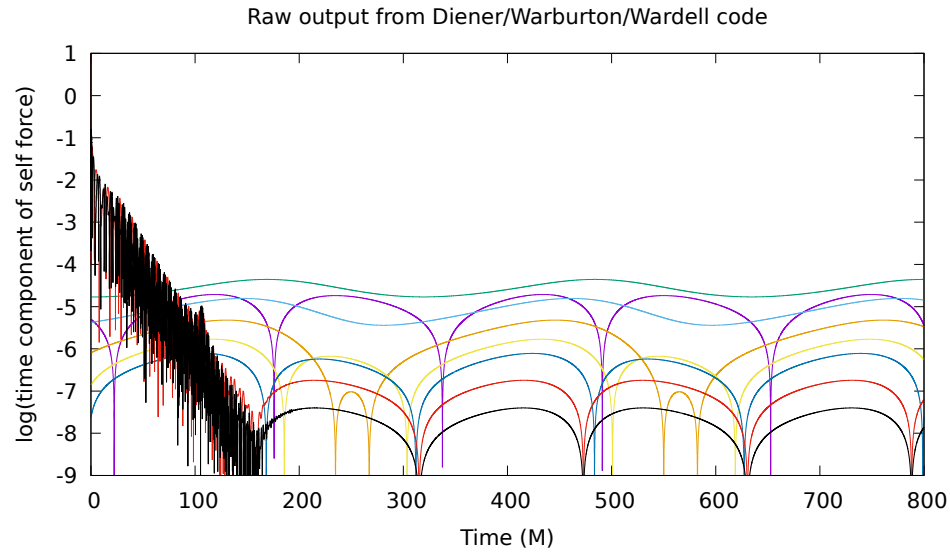
Figure 5.6: Raw output of Diener, Warburton, and Wardell code for DG order 44. Time component of the self force.
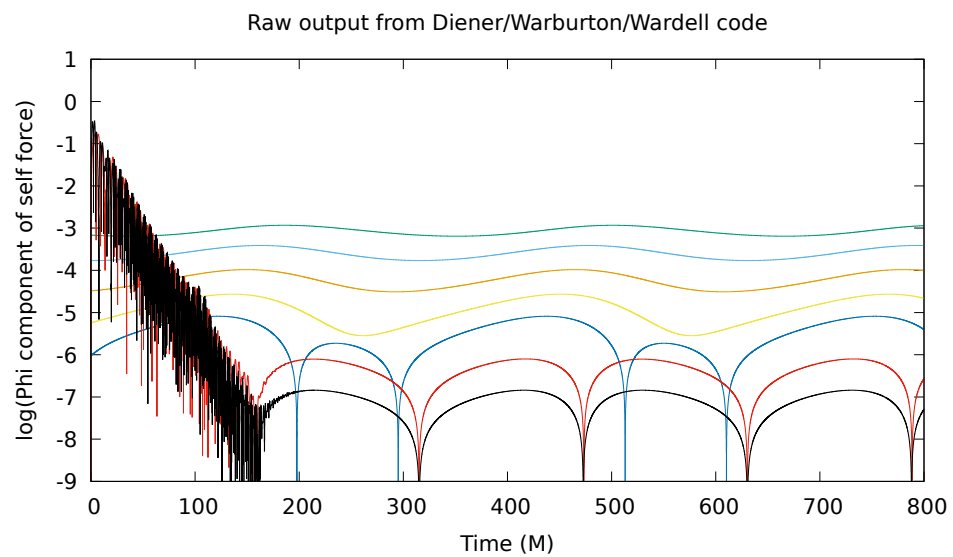
Figure 5.7: Raw output of Diener, Warburton, and Wardell code for DG order 44. Phi component of the self force.

Chapter 6
Extrapolating the self force to infinite Disctontinuous Galerkin order

The Discontinuous Galerkin method results in truncation error that scales as h^{N+1}, where h is the element size and N is the order of the interpolating polynomials within the element. [51] The radial self force is given by the radial derivative of the scalar field, $F_r = \partial_r \Psi$. However, to obtain this quantity, it is necessary to sum the radial derivatives over all l and m modes. Let $F_l = \sum_{m=-l}^{l} F_{lm}$. Each of these modes, separately, follows the DG convergence scaling laws. It should be possible to extrapolate to infinite DG order based and obtain F_{inf}, the self force for a given l-mode at infinite DG order.

The Lagrange interpolating polynomials that are used as the basis for the Discontinuous Galerkin method may also be used for extrapolation. Consider the case of a three degrees of freedom, for a quadratic polynomial. If $y_i = f(x_i)$ for $i = 0 - 2$ [53],

$$
\begin{aligned}
P(x) = \quad & \frac{(x-x_1)(x-x_2)}{(x_0-x_1)(x_0-x_2)} y_0 \\
& + \frac{(x-x_0)(x-x_2)}{(x_1-x_0)(x_1-x_2)} y_1 \\
& + \frac{(x-x_0)(x-x_1)}{(x_2-x_0)(x_2-x_1)} y_2
\end{aligned}
\tag{6.1}
$$

However, this form of extrapolation is insufficient for the case of a function that is fundamentally exponential in form. Nowhere does it approximate a polynomail. It is necessary to extend the extrapolation to one based upon exponential, rather than polynomial, assumptions about the underlying functional form.

The three-point exponential extrapolation is motivated by our assumption that Discontinuous Galerkin error is one-sided in the truncation error regime– it is not random; hence, the self force more or less monotonically approaches a limit. In the round-off error regime where the error is random, the self-force is no longer monotonically decaying. As long as it

is monotonically decaying, it can be written in the form of $F_r(n,l) = F_\infty(l) + c(l) \exp[-\alpha n]$, where n is the DG order. For a given mode, the three-point extrapolation is given by

$$h = \frac{F_r(n_1,l) - F_r(n_2,l)}{F_r(n_1,l) - F_r(n_3,l)} \tag{6.2}$$

$$g(\alpha) = \frac{\exp[\alpha(n_1-n_2)] - 1}{-1 + \exp[\alpha(n_1-n_3)]} \tag{6.3}$$

$$g(\alpha) - h = 0 \tag{6.4}$$

$$c(l) = \frac{F_r(n_1) - F_r(n_2)}{\exp[-\alpha n_1] - \exp[-\alpha n_2]} \tag{6.5}$$

$$F_\infty(l) = F_r(n_3) - c(l) \exp[-\alpha n_3] \tag{6.6}$$

In the middle step, it is necessary to use the bisection method for root finding, numerically, with the condition that α may never be less than zero since the solution must decay. If the three points are not monotonic, sometimes there is not a solution. I use extrapolation starting orders from the set 12, 16, 20, 24, 28, 32, and 36, with additional data at orders 40 and 44 that may be used as points two and three in the extrapolation. In order to use data from several different DG orders, it was necessary to interpolate between the times at which each order was computed to some desired common set of times, since each order takes a different time that decreases with increasing order so that the grid remains spacelike within a full Runga Kutta timestep. Figure 6.1 shows the form of $g(\alpha)$. From this plot, it is clear why h must be greater than 0.5 in order for $g(\alpha) - h$ to have a root.

Since some modes fail, it is not possible to chose the same starting order for the extrapolation for all modes and all times. The first attempt I made to improve the choice of starting order was to chose the highest starting order for which no lower starting order had been unsolvable. Figure 6.2 shows this approach leads to some discontinuities in the time evolution of F_∞ in some l-modes ($l = 3$ is shown).

To address this concern, I examined the choice of starting order more closely for specific times where discontinuities were present. One example, for $l = 2$ and $t = 632M$, is shown in a Table 6.1. Figure 6.3 shows an example where no solution is found. The roundoff noise

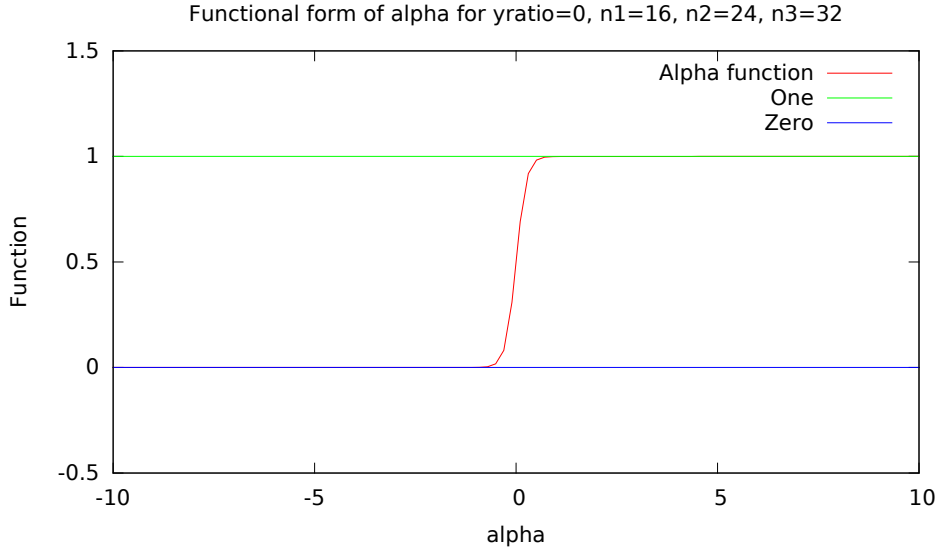Figure 6.1: $g(\alpha)$, h must be greater than 0.5 for the mode and starting order to have a solution at that specific time.
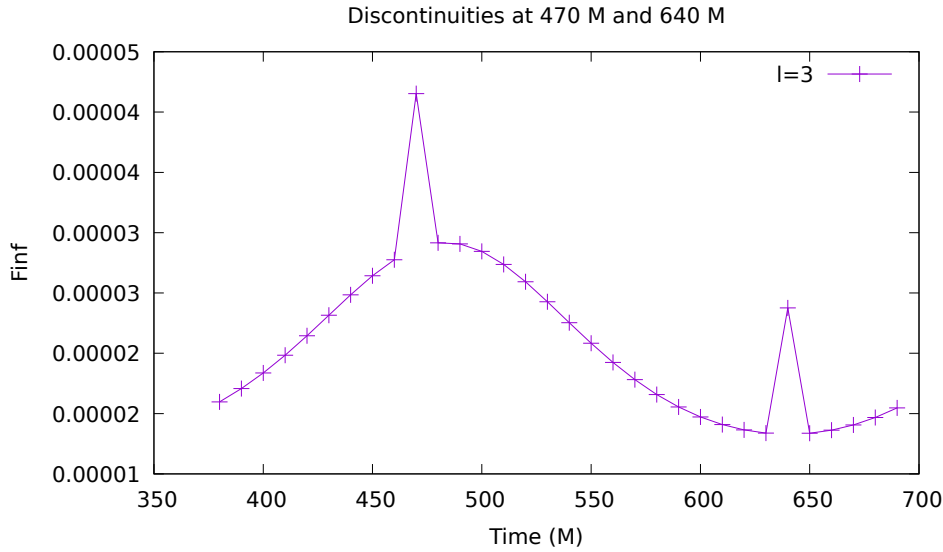

Figure 6.2: Starting order was chosen by iterating from the lowest order to the first order for which the "mode failed", and chosing the maximum starting order that succeded. When F_{inf} is evolved over one full orbital cycle, some l-modes shows discontinuities at some times. l=3

Starting Order	F_∞
0	no solution
1	2.40975299617e-05
2	2.40975300465e-05
3	2.40975300114e-05
4	no solution
5	2.40975299291e-05
6	2.40975299148e-05

Table 6.1: Manual starting indices and F_{inf} values for t=632, l=2.

is visible in Figure 6.4 at high DG orders. In Figure 6.5, it is possible the effect at high DG orders is roundoff noise in the $F_r(n, l)$ values of the points, but it is more likely that it is roundoff noise in the choice of F_∞ due to limitations of the root finding method, resulfing in an incorrect offset of the curve. Figure 6.6 shows that after selecting an average of the reasonably similar values from Table 6.1, the discontinuity in the $l = 2$ $t = 632M$ radial self-force becomes smooth.

6.0.1 Checking for discontinuities in F_{inf} for each each l-mode

In the median approach, the starting orders that had a solution at each time and for each mode are ordered by their F_{inf} values. The median value of F_{inf} is selected, presumably discarding those effected by roundoff and those effected by failure to converge. However, there is no guarantee that it selects those in this regime, since in principle a mode could both be in the roundoff limit and have not converged yet. Yet when this is done, there are no discontinuities in F_{inf} for any of the l-modes when the median approach is used. See mode zero for an example. The maximum or the minimum may also be chosen.

6.0.2 Determining F_{inf} using maximum likelihood fits to subsegments of lines in semilog space

A better motivated approach, is to fit subsegments of lines in semilog space onthe DG order convergence plot, and find the most linear, longest linear, region. A fit with the "best" value of the reduced chi squared should be a good approximation to this. The reduced chi squared is the value of the sum of the residuals of the fit squared divided by
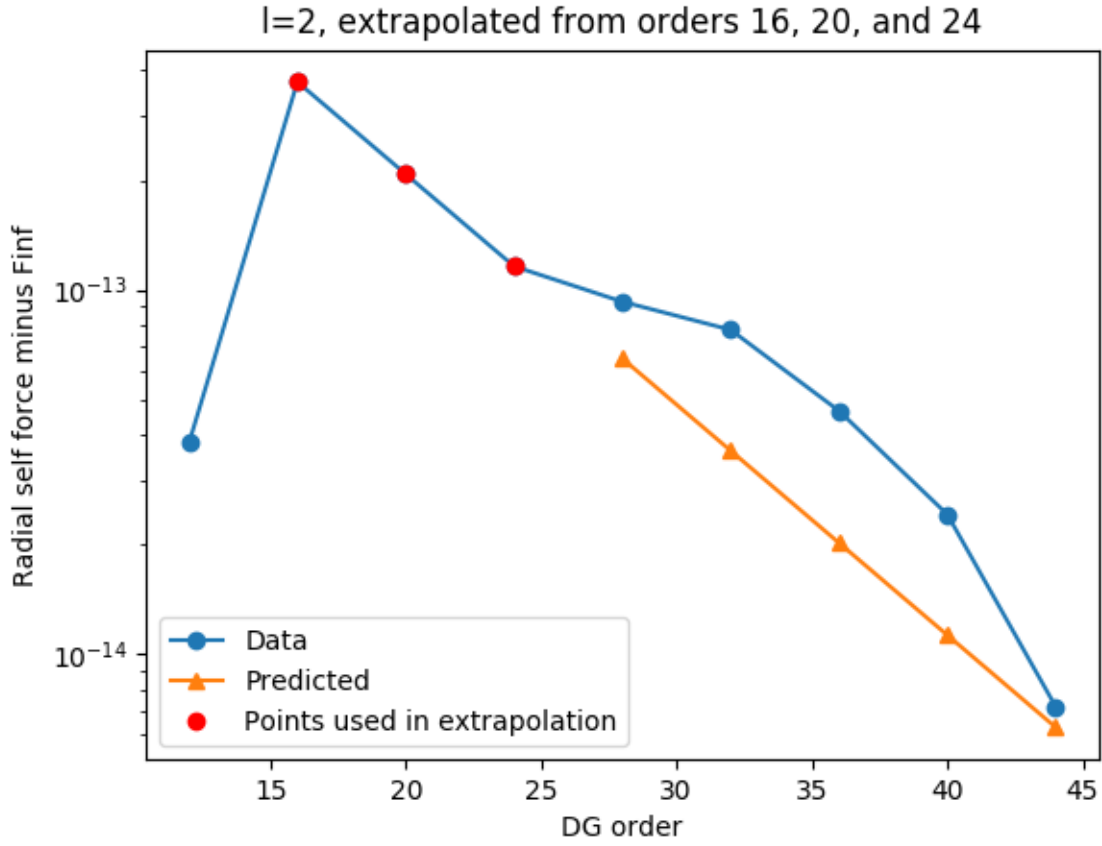
Figure 6.3: Fluctuation in one of the points chosen in the extrapolation, due to roundoff or truncation error, causes the extrapolation to predict a value of F_{inf} that is subtly wrong, leading to curvature in the semilog plot after F_{inf} subtraction. t=632, l=2, i=1
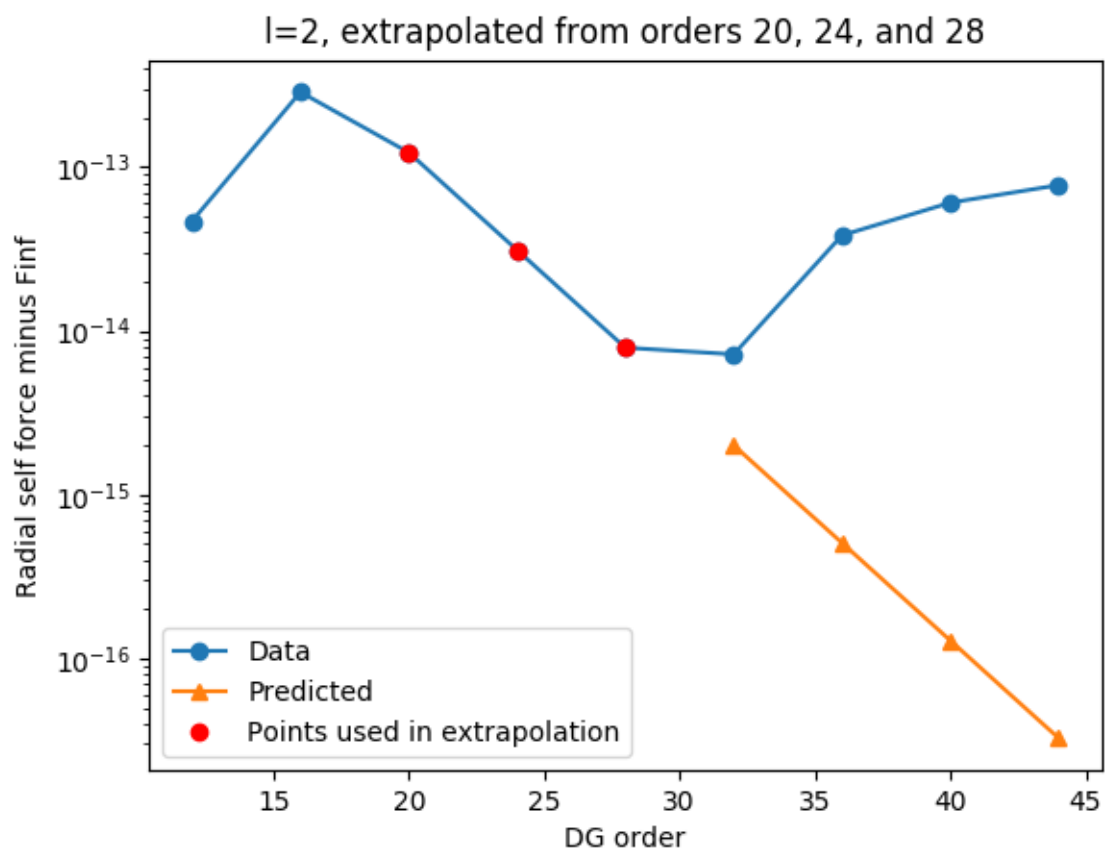
Figure 6.4: Roundoff error is visible at high DG orders. t=632, l=2, i=2
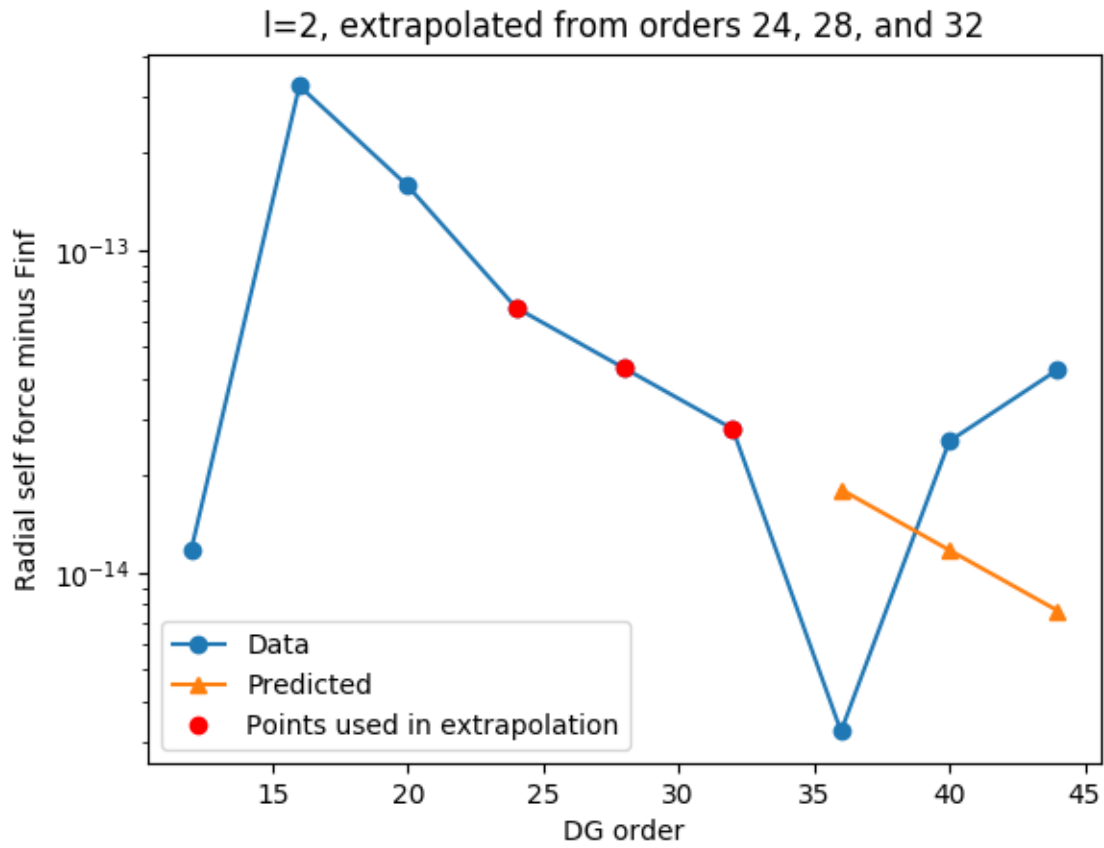
Figure 6.5: The incorrect value of F_{inf} has been chosen due to roundoff error, perhaps due to finite precision in the root finding algorithm, leading to a negative values, that show as a "V" in the semilog plot. t=632, l=3, i=3
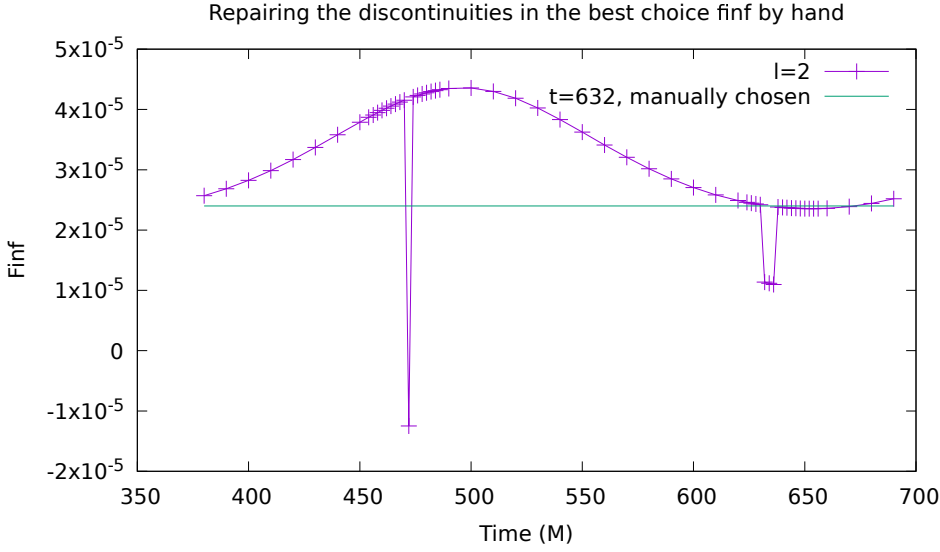
Figure 6.6: Manual correction for the discontinuities in the l=2 mode, using the manually determined F_{inf} data from Table 6.1.

the number of degrees of freedom, which in this case is the number of points in the fit minus two, since there are two degrees of freedom in a linear fit. The expectation value of the reduced chi squared, in the limit of a large number of degrees of freedom, is one. I loop over starting and ending points of the fit, and over starting orders, and choose the starting order with the best fit line segment in the sense that that line segment has a reduced chi squared closest to one. An example of such an automatically chosen starting index is given in Figure ??, where there is a long exponentially converging region. Figure ?? shows that the absolute error between fit and median techniques increases with l-mode, possibly indicating that roundoff error becomes a more significant factor in the median technique as the l-mode increases, and the fit technique becomes more important.

6.0.3 Verification

We expect that F_∞ should be the limit to which the DG orders are approaching, as order increases. Figure ?? shows F_∞ generated by the fit method and the median method, summed naively without an l-mode fit (see Chapter ??) as a function of time, in comparison to three DG orders. It is clear that there is a large gap between these DG orders and F_∞. I am unsure whether this is because the orders converge slowly to the limit, which seems

40
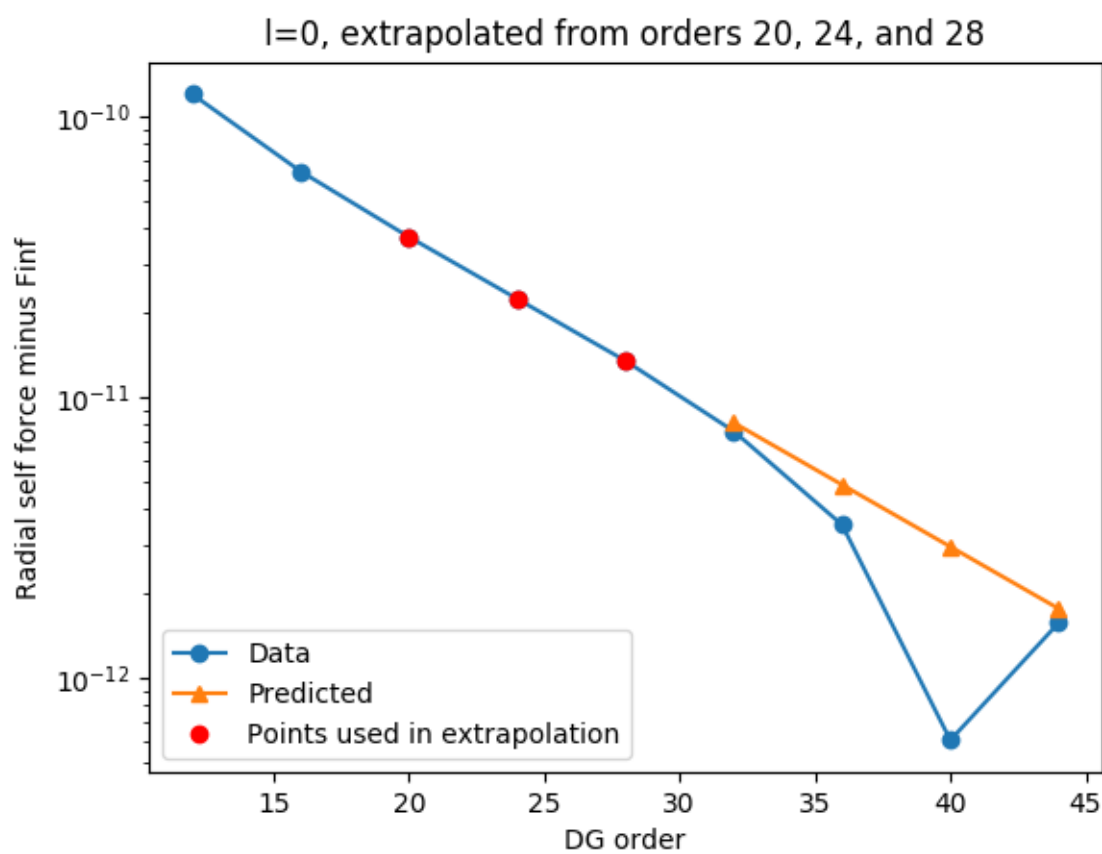
Figure 6.8: l=0 mode with line-segment fit-chosen starting order produces convergence plot with long exponentially converging region
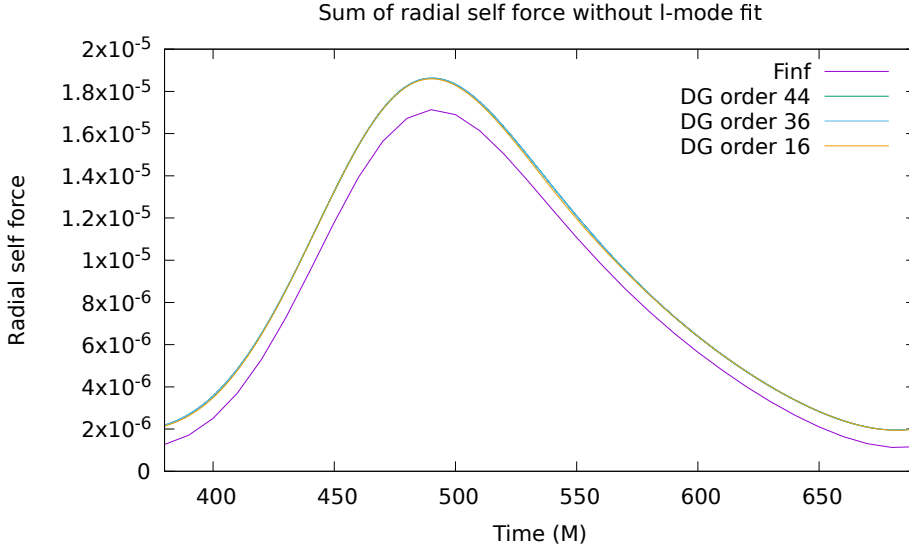
Figure 6.9: A comparison of F_∞ to several DG orders shows that they either do not converge rapidly toward F_∞ or there is a bug in the code.

unlikely since the few orders I have plotted are close together, or because there is a bug in the code. I favor the second hypothesis. The ultimate goal is to choose a suitable DG order with a small enough error relative to F_∞, at which to run all the code in the future.
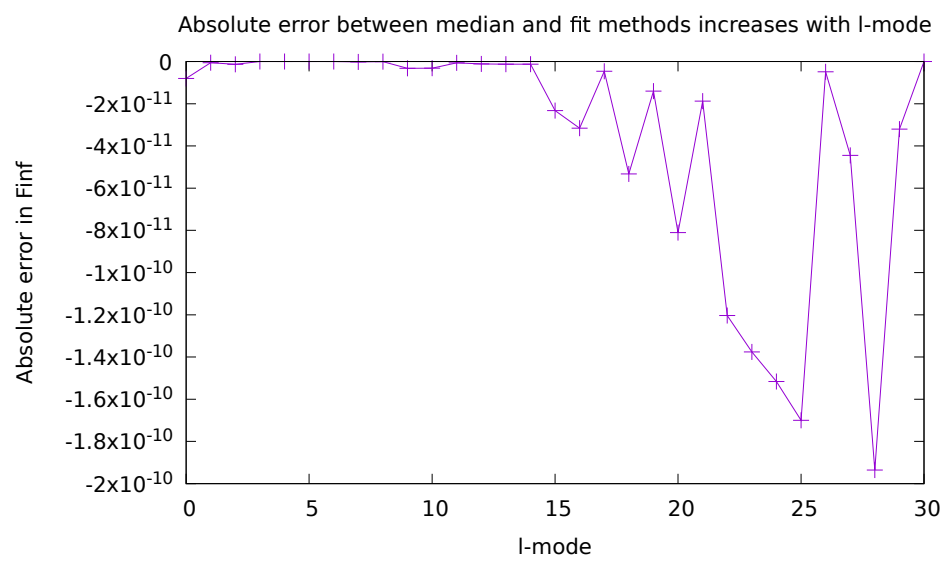
Figure 6.10: Absolute error between fit and median techniques increases with l-mode.

Chapter 7
Extrapolating the mode-summed self-force to include contributions from an infinite number of spherical harmonic modes

In the last chapter, ψ_l was defined as the sum over m within a specific l-mode. To obtain the total self-force, it is necessary to sum all of these l-modes, for every time, using the value of F_∞ selected for that mode. Naively, one might sum only those modes for which there is data– only up to the maximum l-mode computed in the simulation. However, it is possible to do a fit to a functional form found in Reference [13] and use the analytic sum of that functional form to add the contribution from $l_{max}+1$ to infinity to the results computed from the simulation. The dependence of the m-summed self-force for a given mode on l is shown below, modified to omit terms that are rescaled to zero by the definition of the effective source in [?].

$$F_r(l) = \frac{A}{(2l-1)(2l+3)} + \frac{B}{(2l-3)(2l-1)(2l+3)(2l+5)}$$
$$+ \frac{C}{(2l-5)(2l-3)(2l-1)(2l+3)(2l+5)(2l+7)} + \dots \tag{7.1}$$

Here A, B, and C are constants determined by a least squares fit. Least squares fits minimize the sum of the squared differences between the function and the data in the y direction, over all values of x_i. For fit parameters A, B, and C, and $l_max = n - 1$, the portion of the total radial self-force contributed by the l-modes extrapolated to infinity after the end of the known data is given by

$$\sum_n^\infty F_r(l) = \frac{an}{4n^2-1} + \frac{bn}{3(9-40n^2+16n^4)}$$
$$\frac{cn}{5(2n-5)(2n-3)(2n-1)(2n+1)(2n+3)(2n+5)} + \dots \tag{7.2}$$

Although Peter Diener's Fortran code implements this sum, I have analyzed it in an independent way to establish choices of l_{min} and l_{max} and to establish best choice DG orders for the code. In my computations, I have terminated the "end of the known data" at the end of the fit region, on the theory that I am simulating having more or fewer total l-modes available to me by including more or fewer l-modes in my fit.

Figure 7.1 shows a fit including the first three terms of this sum. Note how the fit is bad at high l. There are an infinite number of additional terms that can be added to the fit to account for this deviation. However, it is also fundamentally difficult to fit an exponentially converging function.

7.1 Fitting techniques and choice of starting mode

The quality of the fit depends on the number of terms in the l-mode sum used in the fit, as well as the starting and ending modes chosen. It is also very difficult to fit a nearly power law decay with relative error that does not decrease much at small values, which we might expect as long as the l-modes are in the truncation error regime. This is because a least squares fit minimizes distances between the curve and the data in a linear scale plot, not a log-log plot, giving disproportionate weight to data near the maximum of a power law decay. To correct this, I have suggested an alteration to the fit. I minimize the classic χ^2 with weights, as follows

$$\chi^2 = \sum_i \frac{(y_i - f(x_i))^2}{\sigma_i^2} \tag{7.3}$$

Since the σ_i weights do not represent proper statistical uncertainties, the normalization of the weights is unimportant, unless they are used to interpret the "goodness" of a fit in terms of a reduced chi-squared. Since the error behaves in an unknown, possibly highly correlated, deterministic, manner, cation is warranted in doing so. I have examined weights that are constant (effectively no weight), that scale as l^{-2}, and that scale as l^{-1}. The first is motivated by standard fitting techniques and is the default solution, while the second is motivated by the nature of the first order scaling behavior of the function to which we fit
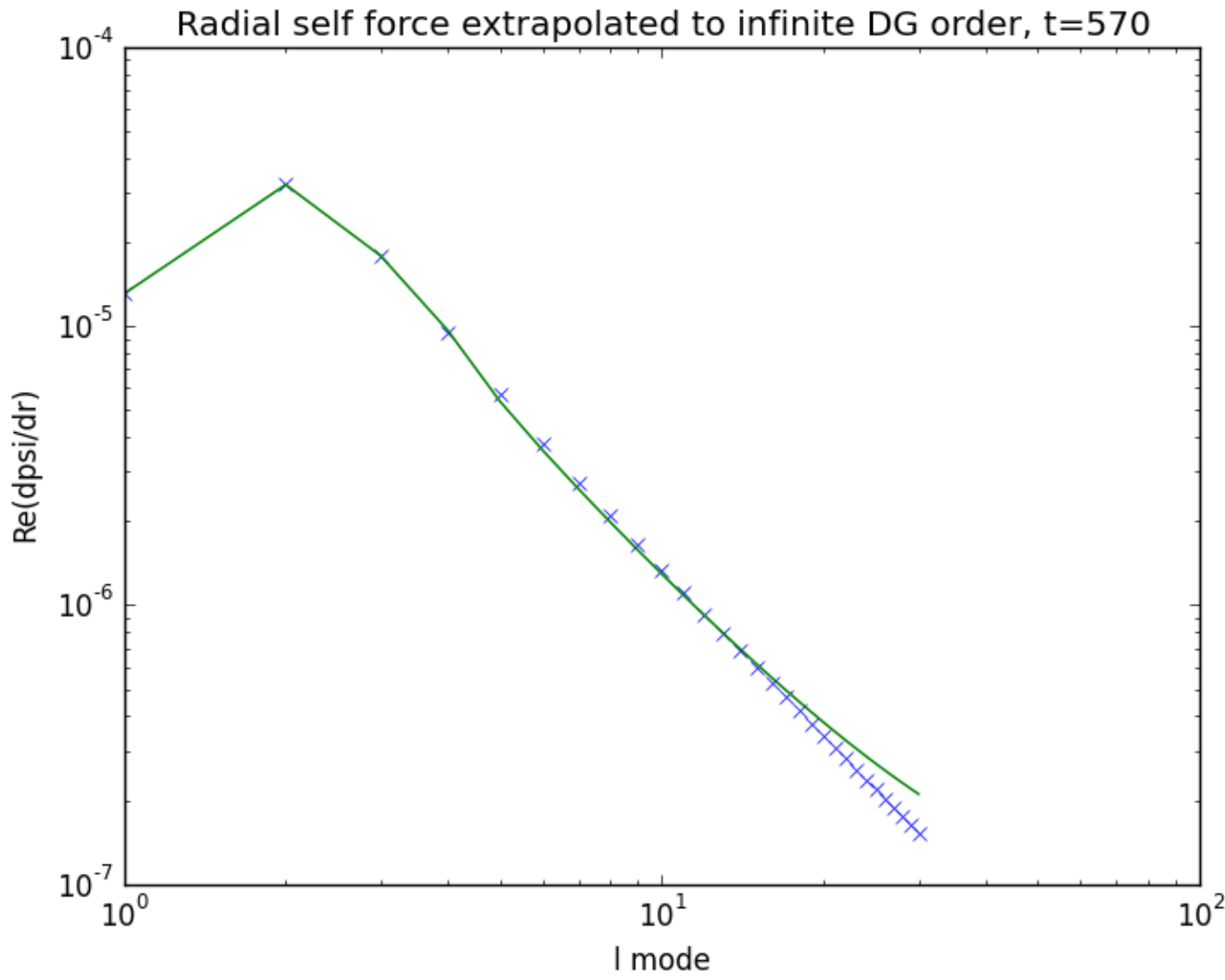
Figure 7.1: Three term fit of l-mode vs F_{inf}.

the l-modes, and the third is motivated by the desire to find something that behaves well in both the truncation error and roundoff error regimes. Figure 7.2 shows the functional form of the l-mode fit with three different choices of weights. Figures 7.3 and 7.4 show that for all choices of weight scaling, a starting l-mode of 14 is a reasonably good fit, while significantly lower starting modes are a bad fit for three terms in the l-mode fit expansion. These figures also show that the choice of sigma can make a small difference in the goodness of the fit at high l-mode, which is important for extrapolation to infinite l-mode. However, Figure ?? shows that for a range of l_{min} versus l_{max}, the variation in the total radial self force due to variation over start and stop range in the fit is small compared to the variation between between l^{-2} scaling and contant scaling (circles and triangles).

7.2 Roundoff noise and choice of end mode

In Figure 7.6 roundoff noise is evident at higher l_{max} choices, where l_{min} is the minimum l-mode included in the fit and l_{max} is the maximum l-mode included in the fit. This is true of most times near aphelion. Note that there is not a large difference between two and three terms, and that four terms is less smooth a surface, suggesting that it is more subject to round off noise. Three terms is preferred. In Figure 7.7, a smaller region of l_min versus l_max space has been chosen to form the surface plot, and the roundoff noise is excluded.

7.3 Results and errors

Figure 7.8 shows the evolution of the total self force over time. First it has been extrapolated to obtain F_∞ using the three-point DG order exponential convergence extrapolation techique, and the optimal starting order has been chosen. Then the modes computed in the simulation have been summed numerically from $l = 0$ up to some l_{max}, and a fit from l_{min} to l_{max} has been used to extrapolate the sum to infinite l, to obtain the total radial self-force, at each time. The three different measurement techniques described
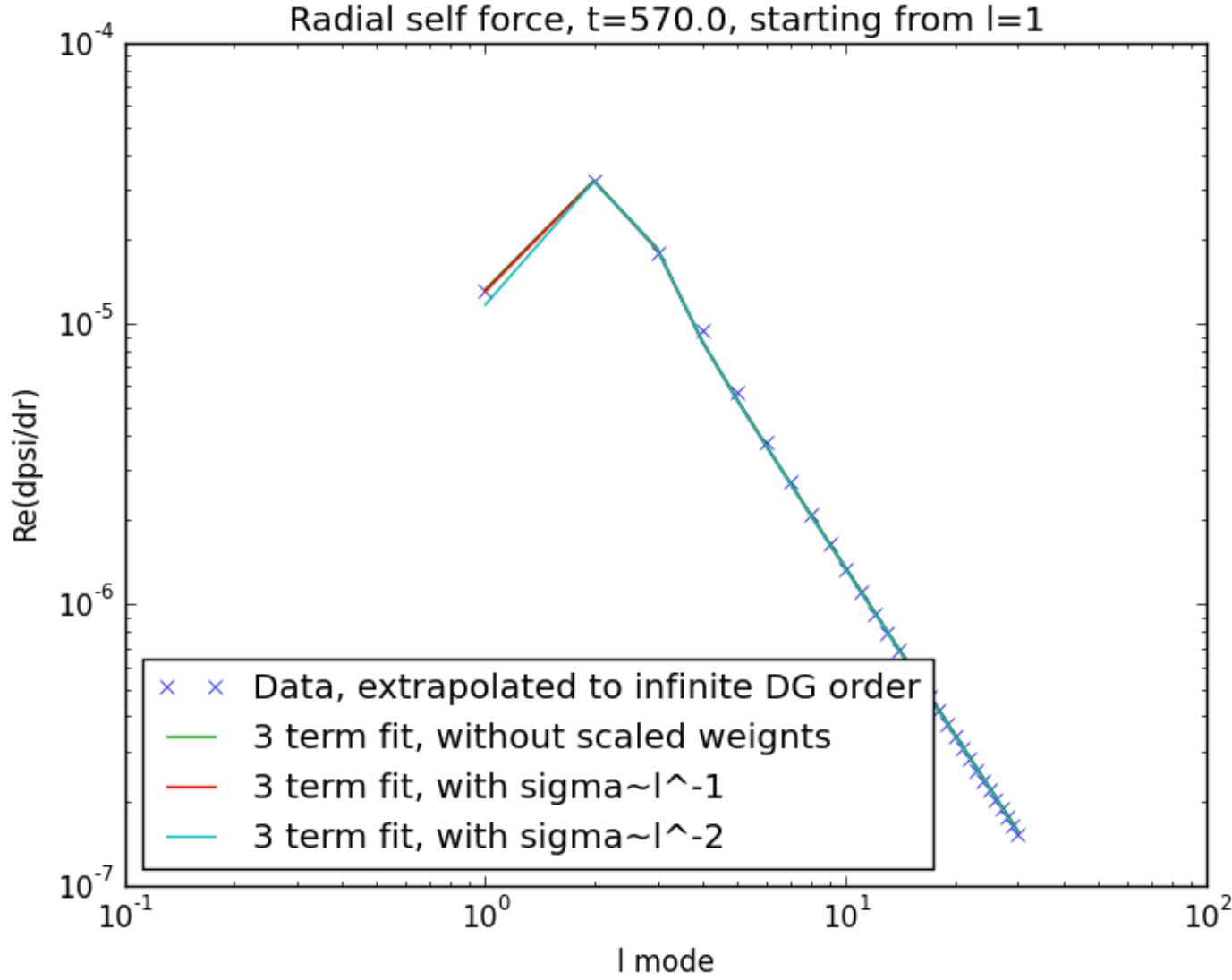
Figure 7.2: The l-mode convergence behavior and three different fits to it using three terms in the l-mode fit sum of Equation 7.1. The three different fits represent different choices of weights in the least squares fit. It appears that starting the fit at 14 might level this residual.
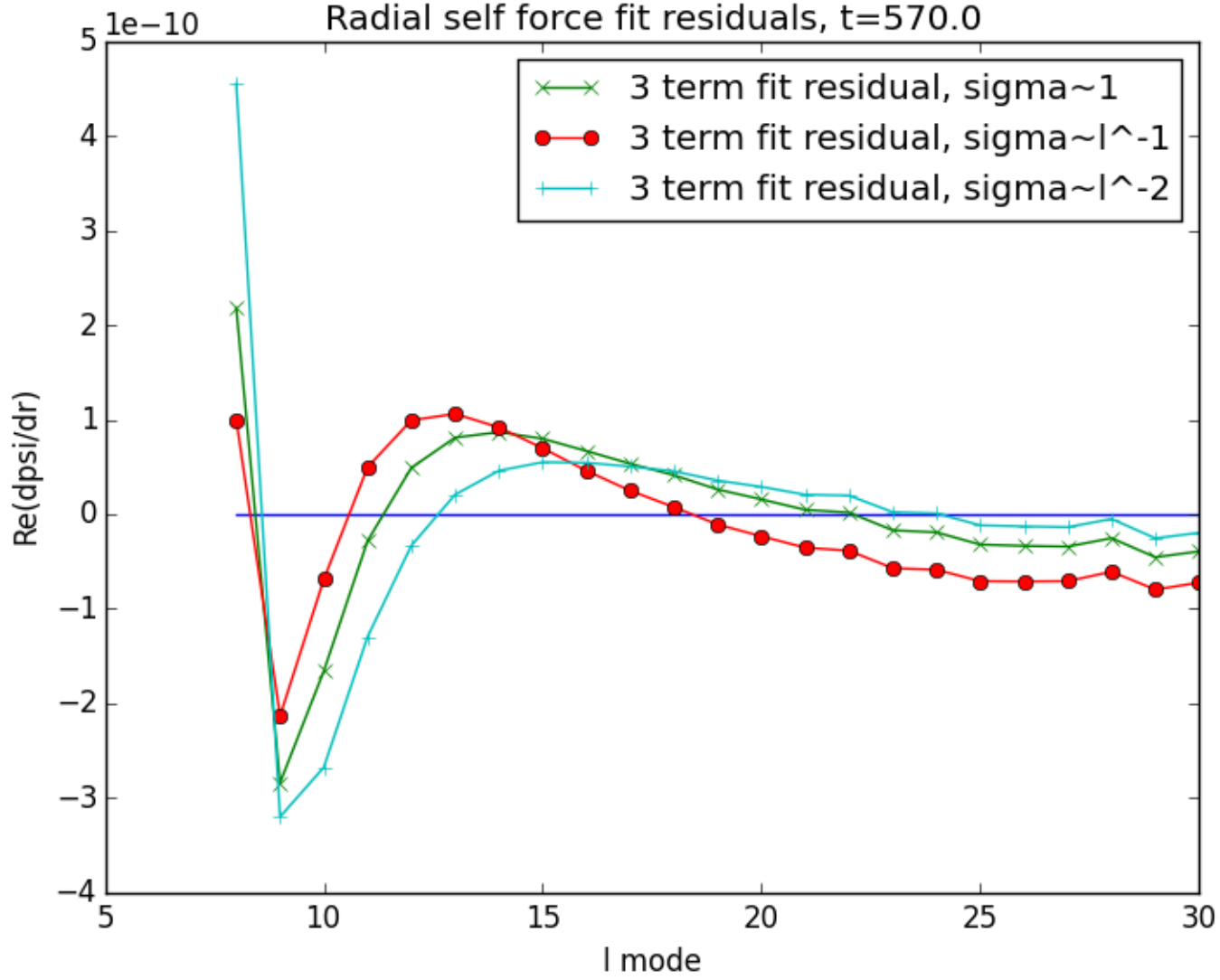
Figure 7.3: Fit residuals for three different least squares weight scalings starting from $l_{min} = 8$. Notice that this is a bad fit, due to the strong correlated skews to either side of the axis.
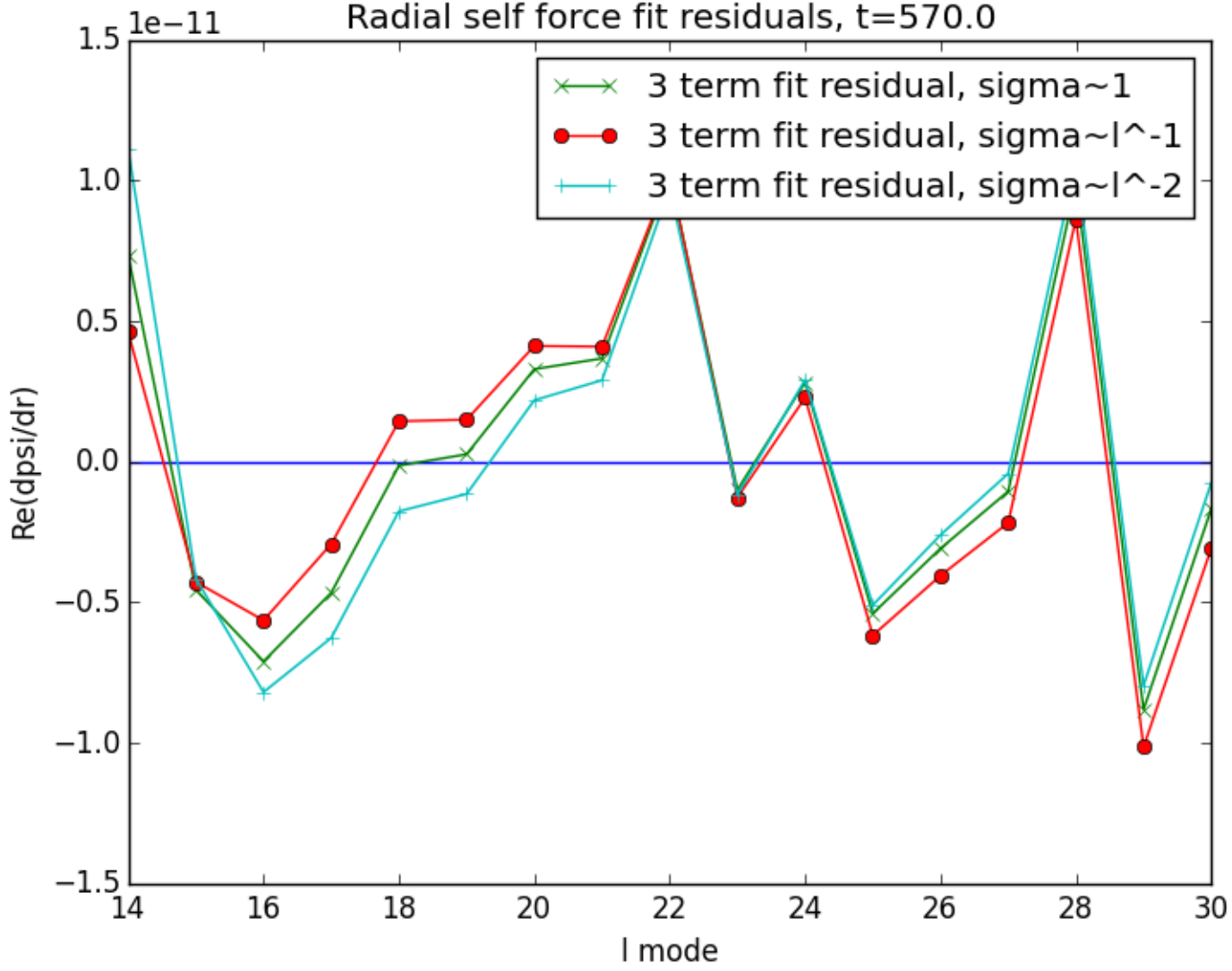
Figure 7.4: Fit residuals for three different least squares weight scalings starting from $l_{min} = 14$. This is a much better fit than $l_{min} = 8$ both due to the smaller correlated deviations from zero and due to the smaller amplitude of the residual.
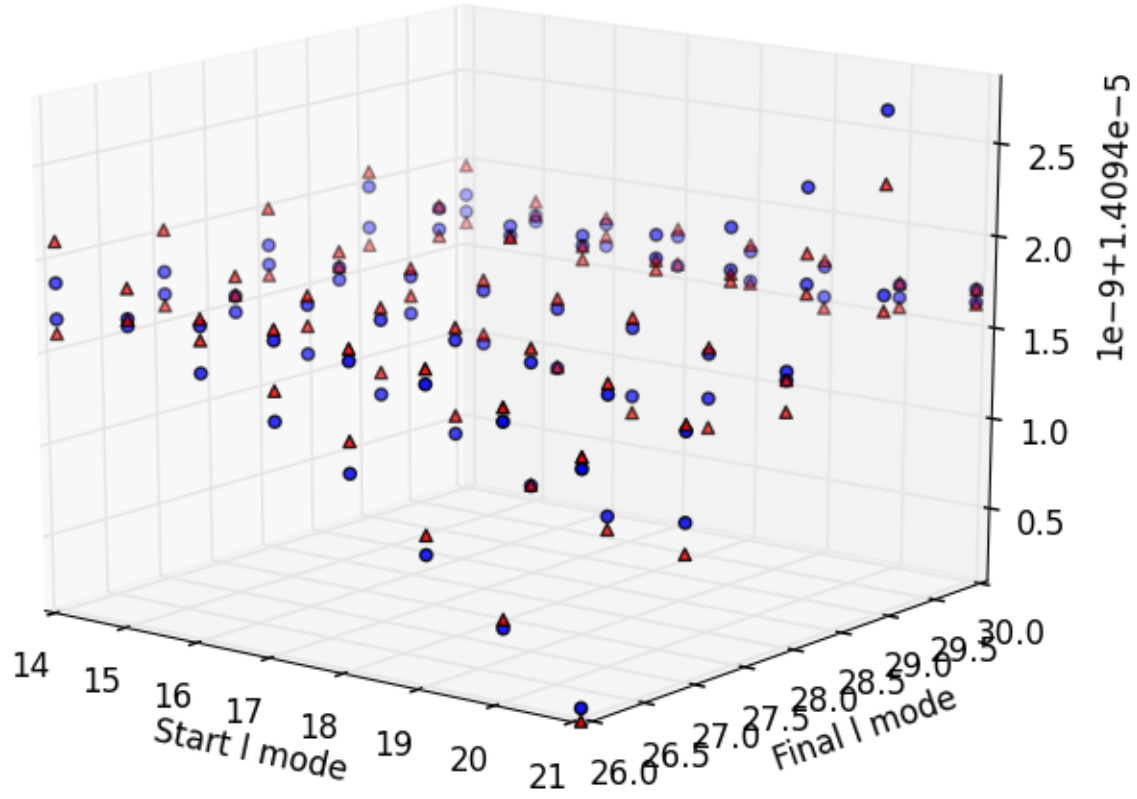
Figure 7.5: The difference between the triangles and the circles shows that the difference in the total radial self force between the presence of a $\sigma \sim l^{-2}$ weight and no weight is unimportant compared to the difference in the total radial self force between various start and end points of the l-mode fit.
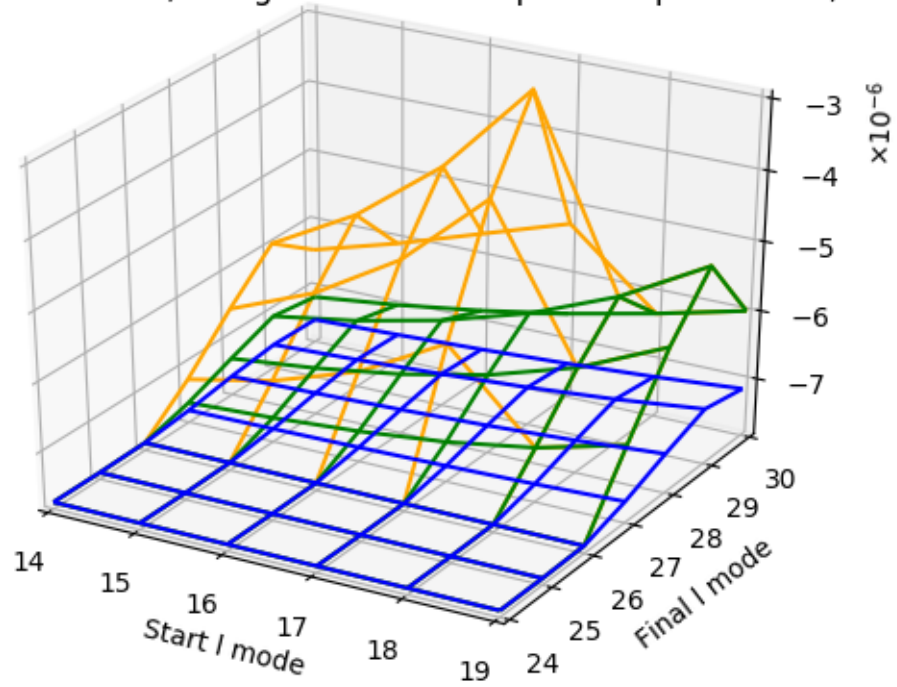
Figure 7.6: t=635, 2, 3, and 4 term fits over a broad range of lmin and lmax values. Note the roundoff noise at high lmax. Aphelion, where this effect is worst.
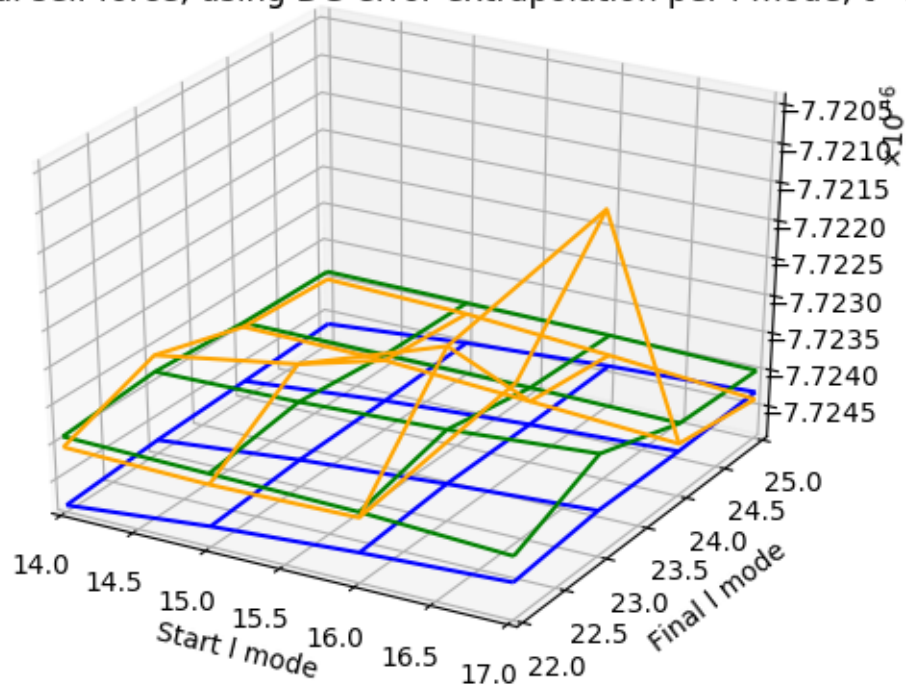
Figure 7.7: t=635, 2, 3, and 4 term fits over a small range of l_{min} and l_{max}. Aphelion. No roundoff noise in this range.
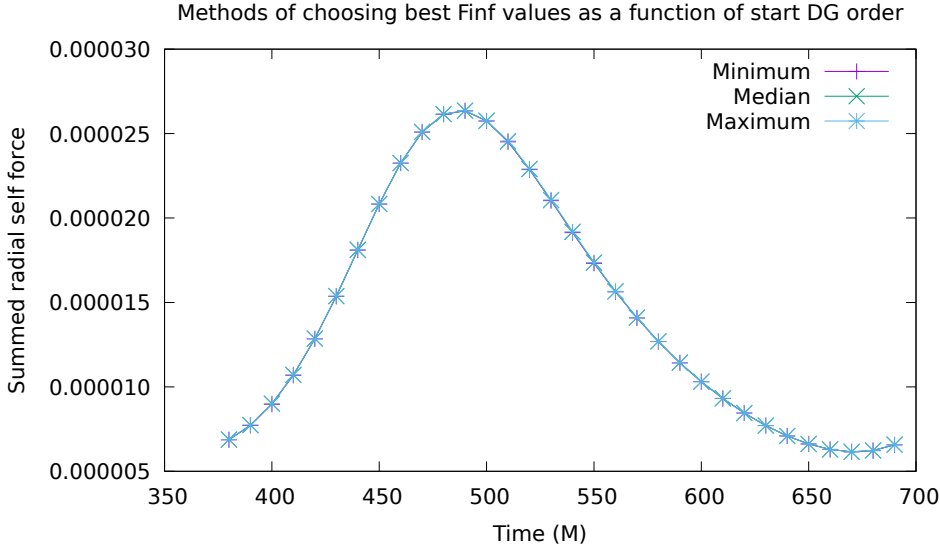
Figure 7.8: This is the actual summed, doubly extrapolated, radial self force, measured using the minimum, maximum, and median method for selecting the best starting order.

7.3.1 Relative and absolute differences

Figure 7.9 shows the relative difference between the total radial self force measured in two different ways. The self-force values in each surface plot shown in Figures 7.6 and 7.7 were averaged to obtain better estimates of the total radial self force as a function of time. This plot shows the relative difference. Some caution is advised in interpretation, since the relative difference may largely point to roundoff noise in the larger range. It is clearly random, and clearly decreasing with time, but also very clearly not at the machine precision level necessary to be roundoff noise.

Figure 7.10 shows the relative difference between using two and three terms in the fit to compute the total radial self force, as a function of time. Again, this is random, decreasing with time, and not at the machine precision level.

In Figure 7.11, the purple line is the relative difference between the maximum and the median, and the green line is the relative difference between the median and the minimum. The first is subject to roundoff error due to the potential for the DG order with the maximum self-force, which is likely the maximum DG order, to contian roundoff error. The second is subject to effects due to failure to hit the regime where the truncation error
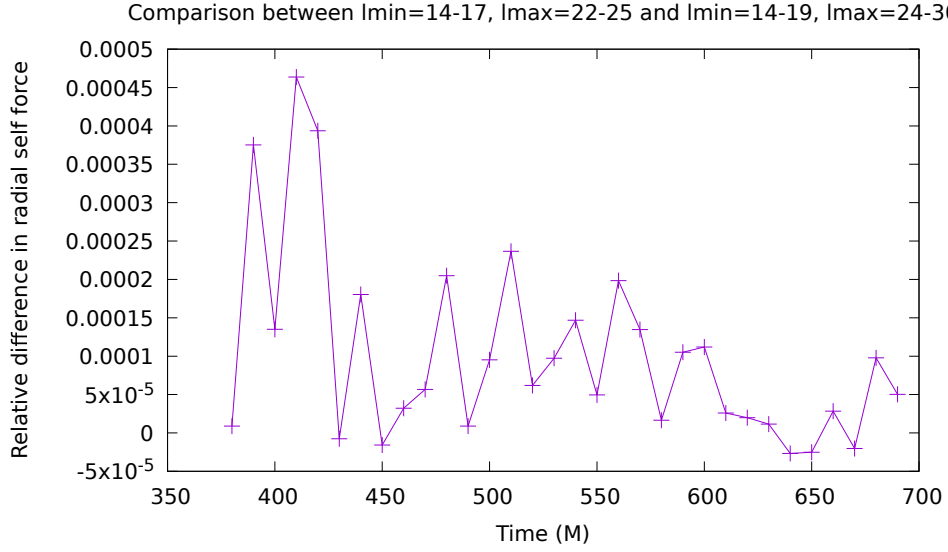
Figure 7.9: The relative difference between total self force determined by averaging large versus small ranges of total radial self-force l_{min}, l_{max} surfaces, as a function of time.
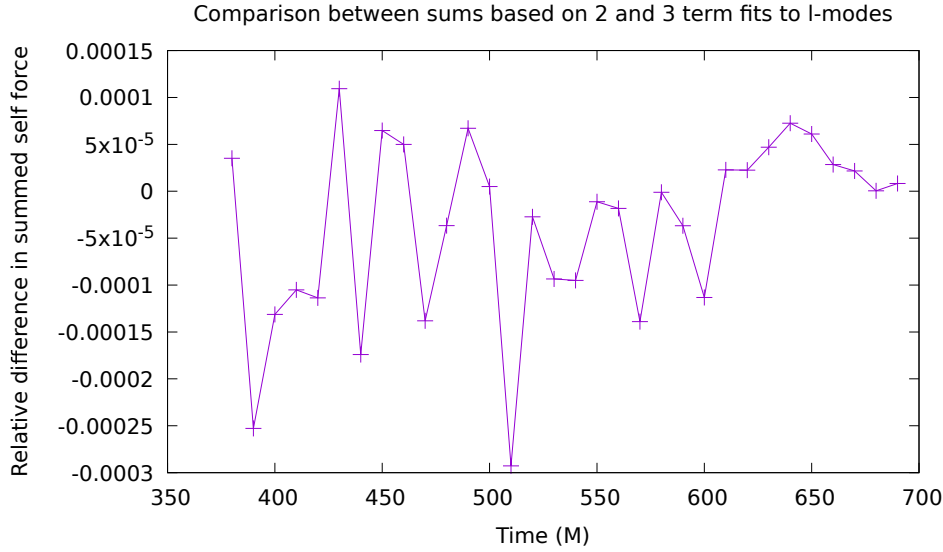
Figure 7.10: The relative error of the total radial self-force, comparing two to three terms in the l-mode fit.

Comparison of results based on different starting orders for extrapolation
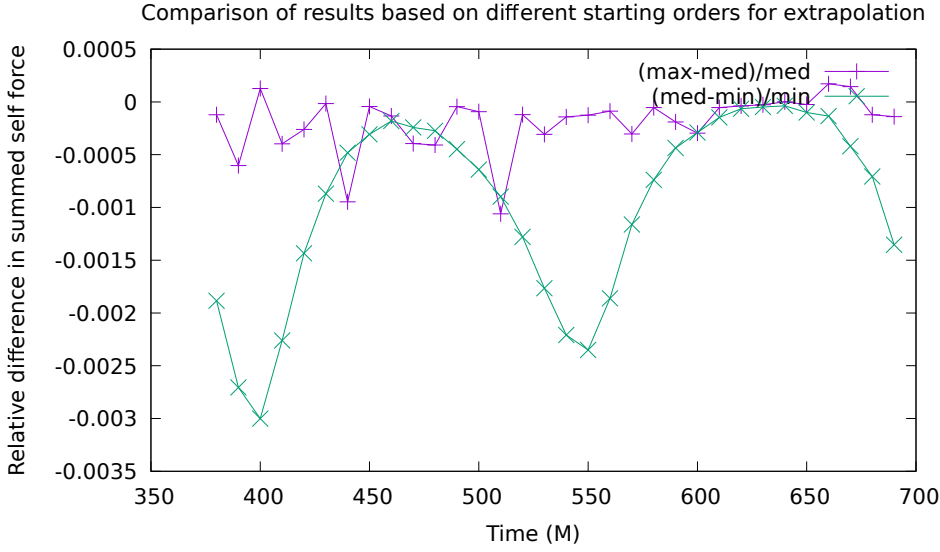
Figure 7.11: The relative error between median, the maximum, minimum methods of determining the starting order, summed over l-mode to obtain the total self-force and evolved over time.

model is valid, because of the minimum.

7.3.2 Fractional errors

I obtain the fractional error, within a given method for choosing the best self force, by dividing the standard deviation of the total self-force, over a range of l_{min} and l_{max} by the average. This is shown for median and fit methods in Figures 7.12 and 7.13, respectively. The absolute error is the standard deviation itself. The absolute error, as a function of time, compared to the self-force itself, is shown in Figure 7.14. The two peaks do not obviously match perihelion, aphelion, or any specific phase of the orbit.

7.4 Best choice l_{mins} and l_{max}'s and best choice DG orders

My conclusion is that l_min can be as low as 14 and as high as 17, and l_max can be as low as 22 and as high as 25 without encountering roundoff or truncation error. There is no single best choice of DG order for a given mode or time, that I have yet been able to establish. It would be quite difficult, in terms of infrastructure, to run multiple DG orders
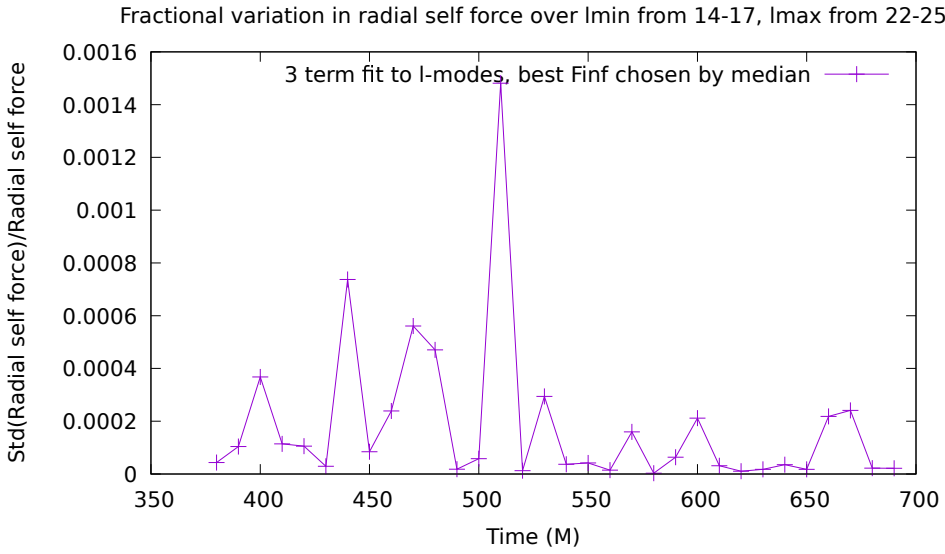
Figure 7.12: Fractional error, 3 term, median method.
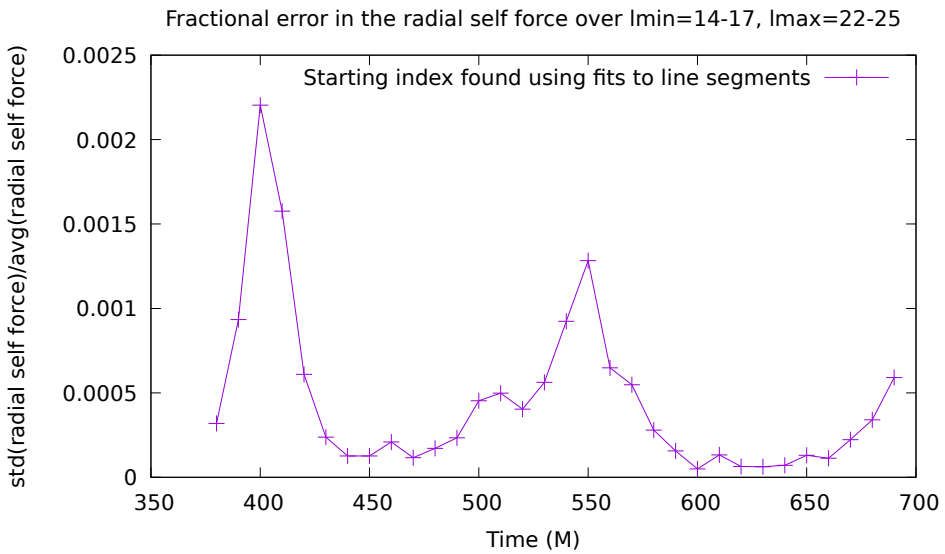
Figure 7.13: Fractional error, 3 term, fit method
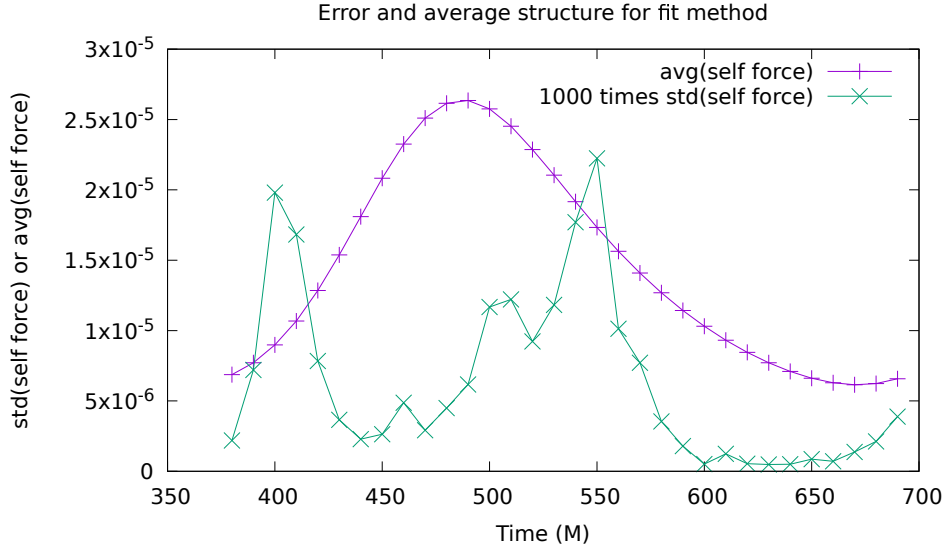
Figure 7.14: The structure of the absolute error in comparison to the evolution in time for the fit method.

at the same time. This work is not yet resolved, and more remains to be done.

The next step is to compare the relative and absolute error of the sum of F_{inf} over each l-mode, without using any mode fit to add the higher modes, to the total self force calculated at the same times (using time interpolation) for several different DG orders, again, without using a fit to extend the sum to higher modes. This comparison could be repeated with the mode fit method for finding the total self-force, for the two different usage cases in the Fortran code.

Chapter 8
Future work: generic orbits via the osculating orbits framework

8.1 plans for the future

going to test Peter Diener's generic orbits and help him develop them further.

$$(\Box - \xi R)\Psi^{ret} = -4\pi q \int \delta_4(x, z(\tau'))d\tau' \tag{8.1}$$

$$ma^\alpha = q(g^{\alpha\beta}_{(0)} + u^\alpha u^\beta)\Psi^R_{,\beta} \tag{8.2}$$

$$\frac{dm}{d\tau} = -qu^\alpha\Psi^R_{,\alpha} \tag{8.3}$$

R is the Ricci scalar (0 in Schwarzchild spacetime) and ξ is the coupling to curvature. The first equation gives th scalar wave equation in curved spacetime, with a source. The second equation gives the back-reaction due to acceleration of the particle. Here, Ψ^R is the regularized field. The third equation governs the self-consistent evolution of the mass of the particle. [32]

8.2 Generic orbits

8.2.1 Geodesic evolution

8.2.2 Osculating orbits

8.2.3 methods

effective source osculating orbits time dependent coordinate transformation world tube already implemented with accelerated orbits though I have not run these. future work: make self consistent evolution work.

8.3   ToDO

He also wants convergence plots of the fit data versus the median data for some bad times. I also want a plot that shows the raw data before the subtraction of the offset for some time. Modify code to use saved raw data.

References

[1] Price, Richard H. (1972). Nonspherical Perturbations of Relativistic Gravitational Collapse. I Scalar and Gravitational Perturbations. *Phys. Rev. D* 5, 10.

[2] Miller, Jeremy; Wardell, Barry; Pound, Adam. (2016). Second-order perturbation theory: the problem of infinite mode coupling. *arXiv:1608.0783v1*.

[3] Heffernan, Anna. (2012). The Self-Force Problem: Local Behavior of the Detweiler-Witing Singular Field. University College Dublin. *arXiv:1403.6177v1*.

[4] Yang, Huan; Zimmerman, Aaron; Zenginoglu, Anil; Zhang, Fan; Berti, Emanuele; Chen, Yanbei. (2013). Quasinormal modes of nearly extremal Kerr spacetimes: spectrum bifurcation and power-law ringdown. *arXiv:1307.8086v1*.

[5] Berti, Emanuele; Cardoso, Vitor; Starinets, Andrei O. Quasinormal modes of black holes and black branes. *arXiv:0905.2975v2*

[6] Philipp, Dennis; Perlick, Volker. (2015). On analytic solutions of wave equations in regular coordinate systems on Schwarzchild background. *arXiv:1503.08101v1*

[7] Diaz-Rivera, Luz Maria; Messaritaki, Eirini; Whiting, Bernard F.; Detweiler, Steven. (2004). Scalar field self-force effects on orbits about a Schwarzschild black hole. *arXiv:gr-qc/0410011v1*.

[8] Diener, Peter; Vega, Ian; Wardell, Barry; Detweiler, Steven. Self-consistent orbital evolution of a particle around a Schwarzschild black hole. *arXiv:1112.4821v3*.

[9] Dirac, P. A. M. (1938). Classical theory of radiating electrons. *Royal Society Publishing*.

[10] Amaro-Seoane, Pau; Gair, Jonathon R.; Pound, Adam; Hughes, Scott A.; Sopuerta, Carlos F. (2014). Research Update on Extreme-Mass-Ratio Inspirals. *arXiv:1410.0958v1*.

[11] Gair, Jonathan R.; Porter, Edward K. (2012). Observing extreme-mass-ratio inspirals with eLISA/NGO. *arXiv:1210.8066v1*

[12] Gralla, Samuel E.; Harte, Abraham I.; Wald, Robert M. (2009). A Rigorous Derivation of Electromagnetic Self-force. *arXiv:0905.2391v2*.

[13] Heffernan, Anna; Ottewil, Adrian; Wardell, Barry; (2013). High-order expansions of the Detweiler-Whiting singular field in Schwarzschild spacetime. *arXiv:1204.0794v4*.

[14] Bernuzzi, Sebastiano; Nagar, Alessandro; Zenginoglu, Anil. (2011). Binary black hole coalescence in the large-mass-ratio limit: the hyperboloidal layer method and waveforms at null infinity. *arXiv:1107.5402v2*.

[15] Danzmann, Karsten. (2017). LISA Laser Interferometer Space Antenna: A proposal in response to the ESA call for L3 mission concepts.

[16] Babak, Stanislav. (2017). Science with the space-based interferometer LISA. V: Extreme mass-ratio inspirals. *arXiv:1703.09722v1.*

[17] Miller, Jeremy; Wardell, Barry; Pound, Adam. (2016). Second-order perturbation theory: the problem of infinte mode coupling. *arXiv:1608.06783v1.*

[18] Mino, Yasushi; Sasaki, Misao; Tanaka, Takahiro. (1996). Gravitational Radiation Reaction to a Particle Motion. *arXiv:gr-qc/9606018v1.*

[19] Yunes, Nicolas; Wofgang, Tichy; Owen, Benjamin J.; Briigmann, Bernd. (2006). Binary black hole initial data from matched asymptotic expansions. *arXiv:gr-qc/0503011v3.*

[20] Poisson, Eric; Pound, Adam; Vega, Ian. (2011). The Motion of Point Particles in Curved Spacetime. *arXiv:1102.0529v3.*

[21] Pound, Adam. (2012). Second-order gravitational self-force. *arXiv:1201.5089v2.*

[22] Pound, Adam. (2017). Nonlinear gravitational self-force: second-order equation of motion. *arXiv:1703.02836v1.*

[23] Pound, Adam; Poisson, Eric. (2008). Osculating orbits in Schwarzschild spacetime, with an application to extreme mass-ratio inspirals. *Phys. Rev. D* 77, 044013.

[24] Quinn, Theodore, C. (2000). Axiomatic approach to radiation reaction of scalar point particles in curved spacetime. *arXiv:qr-qc/0005030v1.*

[25] Quinn, Theodore C.; Wald, Robert M. An Axiomatic approach to electromagnetic and gravitational radiation reaction of particles in curved spacetime. *arXiv:gr-qc/9610053v1.*

[26] Field, Scott E.; Hesthaven, Jan S.; Lau, Stephen R. Discontinuous Galerkin method for computing gravitational waveforms from extreme mass ratio binaries. *arXiv:0902.1287v2.*

[27] Zenginoglu, Anil; Khanna, Gaurav. (2011). Null infinity waveforms from extreme-mass-ratio inspirals in Kerr spacetime. *arXiv:1108.1816v2.*

[28] Vega, Ian; Diener, Peter; Tichy, Wolfgang; Detweiler, Steven. (2009). Self-force with (3+1) codes: a primer for numerical relativists. *arXiv:0908.2138v1.*

[29] Vega, Ian; Wardell, Barry; Diener, Peter. (2011). Effective source approach to self-force calculations. *arXiv:1101.2925v1.*

[30] Vega, Ian; Wardell, Barry; Diener, Peter; Cupp, Samuel; Haas, Roland. (2013). Scalar self-force for eccentric orbits around a Schwarzschild black hole. *arXiv:1307.3476v2.*

[31] Vega, Ian; Wardell, Barry; Diener, Peter; Cupp, Samuel; Hass, Roland. (2013). Scalar self-force for eccentric orbits around a Schwarzschild black hole. *arXiv:1307.3476v2.*

[32] Wardell, Barry. (2015). Self-Force: Computational Strategies. *arXiv:1501.07322v3.*

[33] Wardell, Barry; Vega, Ian; Thornburg, Jonathan; Diener, Peter. (2012). Generic effective source for scalar self-force calculations. *arXiv:1112.6355v3.*

[34] LIGO Virgo Collaboration. (2016). Observation of Gravitational Waves from a Binary Black Hole Merger. *Phys. Rev. Lett.* 116, 061102.

[35] LIGO Virgo Collaboration. (2016). GW151226: Observation of Gravitational Waves from a 22-Solar-Mass Binary Black Hole Coalescence. *Phys. Rev. Lett* 116, 241103.

[36] LIGO Virgo Collaboration. (2017). GW120104: Observation of a 50-Solar-Mass Binary Black Hole Coalescence at Redshift 0.2. *Phys. Rev. Lett.* 118, 221101.

[37] LIGO Virgo Collaboration. (2016). Observing Gravitational-wave Transient GW150914 with Minimal Assumptions. *Phys. Rev. D* 93, 122004.

[38] LIGO Virgo Collaboration. (2016). GW150914: First Results from the Search for Binary Black Hole Coalescence with Advanced LIGO. *Phys. Rev. D* 93, 122003.

[39] LIGO Virgo Collaboration. (2016). The Rate of Binary Black Hole Mergers Inferred from Advanced LIGO Observations Surrounding GW150914. *Accepted Astrophys. J. Lett*

[40] LIGO Virgo Collaboration. (2016). Astrophysical Implications of the Binary Black-Hole Merger GW150914. *Astrophys. J. Lett* 818, L22.

[41] LIGO Virgo Collaboration. (2016). Tests of General Relativity with GW150914. *Phys. Rev. Lett.* 116, 221101.

[42] LIGO Virgo Collaboration. (2016). GW150914: Implications for the Stochastic Gravitational Wave Background from Binary Black Holes. *Phys. Rev. Lett.* 116, 131102.

[43] LIGO Virgo Collaboration. (2016). Calibration of the Advanced LIGO Detectors for the Discovery of the Binary Black-hole Merger GW150914. *Submitted to Phys. Rev. D.*

[44] LIGO Virgo Collaboration. (2016). Characterization of Transient Noise in Advanced LIGO Relevant to Gravitational Wave Signal GW150914. *Class. Quant. Grav.* 33, 134001.

[45] LIGO Virgo Collaboration and ANTARES and IceCube Collaborations. (2016). High-energy Neutrino Follow-up Search of Gravitational Wave Event GW150914 with ANTARES and IceCube. *Phys. Rev. D* 93 122010.

[46] LIGO Virgo Collaboration. (2016). GW150914: The Advanced LIGO Detectors in the Era of First Discoveries. *Phys. Rev. Lett.* 116, 131103.

[47] LIGO Virgo, ASKAP, BOOTES, Dark Energy Survey and Camera, GW-EM, Fermi GBM and LAT, GRAWITA, INTEGRAL, IPTF, InterPlanetary, J-GEM, La Silla-Quest, Liverpool Telescope, LOFAR, MASTER, MAXI, MWA, PAN-STARRS, PESSTO, PI of the Sky, SkyMapper, Swift, TAROT, Zadko, Algerian National Observatory, C2PU, TOROS, and VISTA Collaborations. (2016). Localization and Broadband Follow-up of the Gravitational-wave Transient GW150914. *Astrophys. J. Lett.* 826, L13.

[48] Bambi, Cosimo. (2017) Testing black hole candidates with electromagnetic radiation. *Reviews of Modern Physics* 89.

[49] Martynov, D.V., et al. (2016). Sensitivity of the Advanced LIGO detectors at the beginning of gravitational wave astronomy. *Phys. Rev. D* 93, 112004.

[50] Poisson, Eric; Pound, Adam; Vega, Ian. (2011). The motion of point particles in curved spacetime. *Living Reviews in Relativity.* 14, 7.

[51] Hesthaven, Jan S.; Warburton, Tim. (2008). *Nodal Disconintuous Galerkin Methods: Algroithms, Analysis, and Applications.* Springer.

[52] Saulson, Peter R. (1994). *Fundamentals of Interferometric Gravitational Wave Detectors.* World Scientific Publishing Co.

[53] Press, William H.; Teukolsky, Saul A.; Vetterling, William T.; Flannery, Brian P. (2002). *Numerical Recipes in C++: The Art of Scientific Computing.* The Press Syndicate of the University of Cambridge.

[54] Wolfram, Stephen. (2016). *An Elementary Introduction to the Wolfram Language.* Wolfram-Media, inc.

[55] Newman, Mark. (2013). *Computational Physics.* University of Michigan.

[56] Wald, Robert M. (1984). *General Relativity.* The University of Chicago.

[57] Carroll, Sean M. (2004). *An Introduction ot General Relativity Spacetime and Geometry.* Addison Wesley.

[58] Misner, Charles W.; Thorne, Kip S.; Wheeler, John Archibald. (1973). *Gravitation.* W. H. Freeeman and Company.

Vita

My past research has been on comet photometry, x-ray bursts, gravitational lensing and cosmology, exoplanets, neutrino oscillations, theoretical particle physics, gravitational waves, gravity gradient noise, and fractional calculus. Most of my background is in simulation, whether statistical or theoretical. I think of myself as a computational physicst and a multimessenger astrononomer.

I have 27 publications or preprints thanks in part to my membership in the LIGO Scientific Collabroation from 2009 to 2011. I made significant contributions to five of these, four related to LIGO and one related to exoplanets. I have also had the opportunity to submit, unsucessfully, an additional first author paper on the simulation of order circuit devices with Gary Bohannan at Saint Cloud State University.

Now I am a fourth year graduate student at Louisiana State University, exactly were I intended to be. I have worked on LIGO during the time of three detections. I have had the opportunity to gain experience with multiple techniques for speeding up code with supercomputers in my classes. I have done a little research involving databases and and more involving numerical algorithms. I have the opportunity to continue to contribute to the field of general relativity and to participate in a department where my broad background in the connections between various fields of astronomy is valued. I have helped supervise undergraduate research progress and made a lesson plan for and taught a graduate class, once. This document contains the research I have produced in the last three years since I arrived on June 3, 2014 at LSU and began working with Peter Diener. These have been the best three years of my life.

When interpreting the name on this document, please understand that I am female to male transgendered and that my legal name is Susan Elaine Dorsher but that I go by Steven James Dorsher.